Are superconductivity mechanisms a matter for chemists?

Michel Pouchard, Antoine Villesuzanne

Are superconductivity mechanisms a matter for chemists?

Michel Pouchard* and Antoine Villesuzanne

CNRS, Univ. Bordeaux, Bordeaux INP, ICMCB, UMR 5026, F-33600 Pessac, France

*corresponding author : Prof. Michel Pouchard, ICMCB-CNRS, 87 Av. Dr. A. Schweitzer, 33608 Pessac Cedex, France

Abstract.

From a tight-binding approach of the instability of non-bonding electron states, along a double-well potential, we consider here how the coupling with a phonon mode can open a gap at Fermi level. The alternation of broken- and unbroken symmetry, along the phonon breathing distortion, induces the mixing of band-edge states on very short timescale, according to chemist' non-crossing rule. We show that this mixing may generate cationic as well as anionic disproportionation. The negative *U* mechanism is thus justified here, leading to the mixing of occupied and unoccupied pair states, for the opening of a 2*Δ* superconducting gap. The vicinity of broad σ* and narrow π* bands should favor the superconducting phase, with respect to the insulating or metallic ones, in agreement with Micnas et al.'s works. We applied this approach to several families of superconducting materials, i.e. doped strontium titanate, high-T_C cuprates and iron selenide.

Keywords: Non-bonding electrons; Non-crossing rule; Negative-*U* mechanism; Phonons; BCS theory; Disproportionation; Hole pairing; Cuprates; Titanates; Iron selenide.

Introduction.

Are superconductivity mechanisms a matter for chemists? Such a question was a hot topic half a century ago, when the excitonic origin of superconductivity was widely discussed by authors such as Schafroth, Blatt and Butler [1] or Little [2], in terms of strong interactions in real space (r-space, familiar to chemists).

However, the success of the Bardeen-Cooper-Schrieffer (BCS) theory [3] and so-called BCS model, based on a delayed coupling between electrons of opposite spin and momentum, by exchange of phonons in reciprocal space (k-space) - a model that was immediately validated by experiment -, discouraged many chemists to pursue the r-space approach. Actually, the theory predicted an upper value of ca. 30 K for the superconducting transition temperature T_C.

At its early stage, solid state chemistry rather focused on metal-insulator transitions, more spectacular as for example in vanadium oxides in which electric conductivity could vary by more than ten orders of magnitude across the transition [4], and be correlated to small crystallographic changes (r-space).

This is why many new families of solids, discovered by chemists, were only later found superconducting by physicists. In particular, this was the case of the so-called Chevrel phases discovered by Prigent, Sergent and Chevrel [5] in which superconductivity (T_C = 15 K) was evidenced two years later by Matthias [6].

A fourteen-year gap occurred between the synthesis of the first cuprates +III of lamellar perovskite type (Hagenmuller, Goodenough, Pouchard, and Demazeau [7]) and the discovery of their superconductivity (T_C = 32 K) by Bednorz and Müller [8]; meanwhile, Raveau, Studer and Nguyen [9] had evidenced the key mixed valency +III/+II of copper in these systems.

From then on, chemists participated actively to the so-called « golden rush » for new superconducting families and higher T_C values.

Thirty years later, there is no consensus on the origin of this unconventional, high-T_C superconductivity: (bi-)polaronic, electronic, magnetic, excitonic…? Solving this mystery has been mostly the playground of physicists.

However, a few chemists' concepts were proposed as soon as 1987: copper +II disproportionation (similar to silver +II and gold +II) and oxygen to copper charge transfer [10-12], which remained disregarded.

In 1990, Micnas, Ranninger and Robaczkiewicz [13] published a paper titled "superconductivity in narrow band systems with local non retarded attractive interactions" that grabbed the attention of A. Simon with regards to the properties of his rare-earth halogeno-carbides [14]. Actually, Micnas et al. provided an intermediate model, mixture of local pairs and itinerant electrons interacting via a charge-exchange mechanism, giving rise to a mutually induced superconductivity in these systems.

Among popular topics in today's physics is found the relations between three types of order, namely magnetism (spins), ferroelectricity (charges) and superconductivity (Cooper pairs); an example is multi-ferroïcity. Solid state chemistry and its conceptual framework (structure-bonding-properties) is intrinsically involved in these three important types of ordering.

In this article, we present a chemist' approach of the effect of doping in $SrTiO_3$, which progressively turns from a quantum ferroelectric insulator to a metal and a superconductor, as recently presented by Rischau et al. [15], and Gabay and Triscone [16].

Then, while developing some of our previous works [17], we describe features underlying the transition from an antiferromagnetic Mott-type insulator such as La_2CuO_4 into a high-T_C superconductor.

Finally, we tentatively apply these approaches to another family of high-T_C superconductors, the iron pnicto/chalcogenides [18,19].

2. A chemist's scenario.

2.1. Non-bonding electrons, from single to double well.

Cohesive energies in an iono-covalent solid can be described by a unique potential well, of Lennard-Jones form, with three terms arising from long-range Coulomb forces, short-range van der Waals (attractive) and Born forces (repulsive). As a function of the inter-atomic distance d, these three terms vary as d^{-1}, d^{-6} and d^{-12}, respectively. A covalent bond, for which the potential well has a single minimum as a function of d, can be viewed as a charge accumulation in the inter-atomic region.

An atomic orbitals (AO) basis set is often used to express the electronic structure, i.e. to expand molecular or crystal orbitals. From a molecular or local viewpoint, non-bonding electrons (NBE) refer to molecular orbitals built on AOs with a vanishing overall overlap S. Overlap can be very small alike in δ-type bonding (for example, xy-xy along the z direction) or vanish globally by symmetry, as shown hereafter in CO_2.

2.1.1. Point symmetry and the CO_2 molecule.

For a CO_2 molecule oriented along *z*, let us examine π-type molecular orbitals built on $2p_x$ AOs of carbon and oxygen atoms (labelled O1 and O2). A bonding, a non-bonding and an antibonding molecular orbital, respectively noted $1\pi_u$, π_g and $2\pi_u$, arise from the three $2p_x$ AOs (Figure 1a). The non-bonding character of π_g results from the exact compensation of $2p_x$-$2p_x$ overlap integrals *S*: *S*(C-O1) = -*S*(C-O2) when the *gerade* combination of O1 and O2 $2p_x$ orbitals is considered.

If the symmetry is lowered by a displacement of the carbon atom with respect to the center of symmetry, as in a vibration mode, this molecular orbital will no longer be non-bonding, since the overlaps no longer compensate. The amplitude of the vibration mode depends on the shape of the potential well for the covalent bond, but also on the atoms polarizability (related to Pearson's hardness in soft/hard chemistry concepts).

2.1.2. Translation symmetry and reciprocal space.

The non-bonding character of a crystal orbital can arise from translation symmetry, for a given point or direction in the Brillouin zone. For a regular $(TiO)_\infty$ chain in $BaTiO_3$ along the *c* direction of the lattice, according to a tight-binding approach, some crystal orbitals are built on combinations of O $2p_x$ and Ti d_{xz} AOs. Among its quantum numbers, each crystal orbital $\varphi_{\boldsymbol{k}}$ is characterized by a wave vector ***k*** that belongs to the first Brillouin zone. If we restrict our example to a one-dimensional chain, then *k* is a wave number with $-\pi/c < k < \pi/c$ and

$$\varphi_k(\boldsymbol{r}) = \sum_n e^{iknc} . \{c_1(k) . d_{xz}(\boldsymbol{r}) + c_2(k) . 2p_x(\boldsymbol{r})\} \qquad [1]$$

where integer n indexes the unit cells, *c* is the lattice parameter, c_1 and c_2 are normalized coefficients that depend on *k*.

Figure 1b shows the schematic energy diagram (or dispersion curves) $E(\varphi_k)$ vs. ***k*** for the two levels or bands arising from the two AOs $2p_x$(O) and d_{xz}(Ti). At the zone center Γ (***k*** = 0), $2p_x$ and d_{xz} are not symmetry compatible and crystal orbitals φ_k are respectively of pure $2p_x$ (top of valence band) and pure d_{xz} (bottom of conduction band) character. The most bonding (resp. antibonding) combinations are found at the zone boundaries ($|\boldsymbol{k}| = \pi/c$). Therefore, non-bonding states are found at the zone center, with energies of single O $2p_x$ and Ti d_{xz} AOs, respectively.

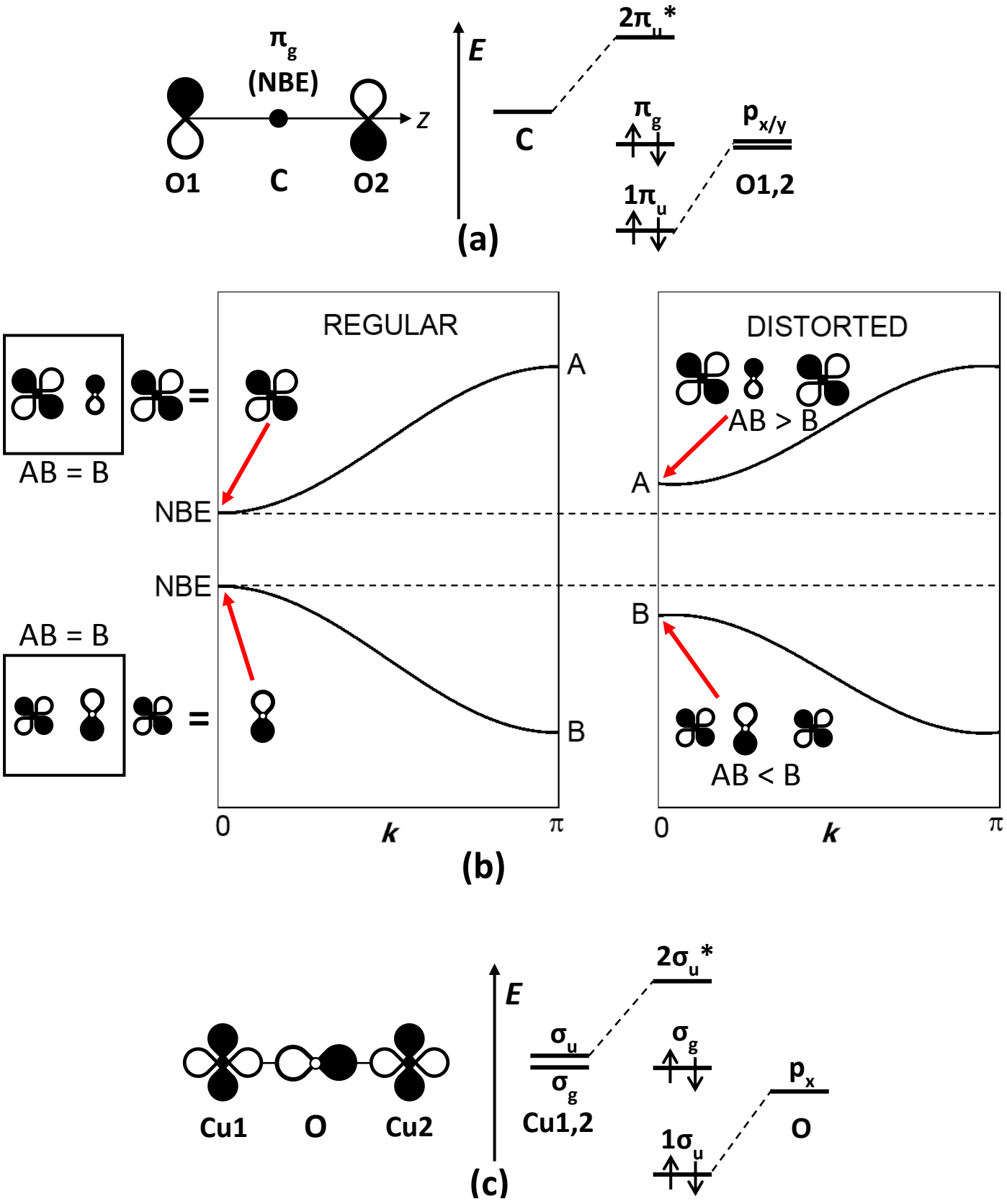

Figure 1. Non-bonding electrons. (a) By point-symmetry compensation: non-bonding π_g molecular orbitals of CO_2. (b) By translational symmetry compensation: non-bonding crystal orbitals of a $(TiO)_\infty$ chain. (c) Non-bonding spin-orbital σ_g for a fragment Cu_2O in a $(CuO)_\infty$ chain.

Any phonon mode displacing the oxygen atom along *c*, i.e. shortening vs. lengthening Ti-O bonds, allows bonding and antibonding Ti-O interactions to build up at the top of the valence band and at the bottom of the conduction band, respectively, at Γ. Consequently, the band gap increases and non-bonding states no longer exist at the band edges. In this case, the Lennard-Jones potential $E(q)$ centered on the equilibrium distance (q = 0) superimposes with an off-centered potential $E'(q)$. The q = 0 position is metastable for $E(q)+E'(q)$, which has a double-well shape. The double-well depth depends on the magnitude of short-range Born forces, oxygen ion polarizability, and overlap/transfer integrals.

According to the double-well depth, several behaviors arise: i) the freezing of the phonon mode, into a ferroelectric-type distortion, ii) an oscillation of the oxygen position, of "transient crystal structure"-type, or iii) the tunneling between the two potential wells, for small depth values. This approach was discussed recently by Gabay and Triscone as previously quoted [16], following a former description of the ferroelectric instability on the basis of chemical bonding, found in the textbook "Chemical Bonding in Solids" by J. K. Burdett and in a previous paper by R. Hoffmann et al. [20].

2.1.3. Multielectron systems: Hartree-Fock-Roothan spinorbitals.

For a $[Cu_2O]^{2+}$ entity in a $(CuO)_\infty$ chain, two combinations of copper x^2-y^2 orbitals are possible, i.e. $(x^2\text{-}y^2)_1 \pm (x^2\text{-}y^2)_2$, where indices 1 and 2 refer to the two copper atoms. The sum and difference of x^2-y^2 orbitals have gerade (g) and ungerade (u) symmetry, respectively.

Only the u combination allows a mixing with oxygen $2p_x$ orbital, giving a bonding ($1\sigma_u$) and an antibonding ($2\sigma_u$*) molecular orbital (Figure 1c).

Here, oxygen 2s semi-core orbitals are not considered (see discussion later in part 4.3.3). Then, the g combination of x^2-y^2 orbitals gives a non-bonding molecular orbital (with respect to Cu-O bonding); it is weakly Cu-Cu bonding. This molecular orbital (noted σ_g hereafter) is expressed in the Hartree-Fock-Roothan formalism, using x^2-y^2 orbitals as basis set and according to Deutscher and De Gennes [21]:

$$\sigma_g \propto \left|(x^2-y^2)_1\ \overline{(x^2-y^2)_2}\right| + \left|(x^2-y^2)_2\ \overline{(x^2-y^2)_1}\right| + \left|(x^2-y^2)_1\ \overline{(x^2-y^2)_1}\right| + \left|(x^2-y^2)_2\ \overline{(x^2-y^2)_2}\right| \quad [2]$$

The two first terms are of covalent character and related to the antiferromagnetic coupling between copper sites, of Goodenough-Kanamori type. The two last terms are of ionic character and correspond to a $2Cu^{2+} \rightarrow Cu^{+} + Cu^{3+}$ disproportionation, which was proposed

since 1987 as a possible origin of Cooper pairs in cuprates (as mentioned in the introduction) [10-12], and which is closely related to the Hubbard parameter *U* for electron-electron repulsion. Those ionic terms indicate that, similarly to $BaTiO_3$, a succession of disproportionated states may occur that makes the mid-distance position of oxygen metastable ; due to the difference of ionic radius between Cu^+ and Cu^{3+}, the oxygen atom should move away from the doubly occupied single-site orbital (Cu^+).

As in CO_2, this symmetry breaking allows oxygen $2p_x$ orbital to mix with x^2-y^2 orbitals in σ_g, mostly on the Cu^{3+} site. Phonons will further amplify this symmetry-broken situation, to possibly achieve a permanent distortion at low temperature. Furthermore, cuprates can host other instabilities in which phonons are key parameters, such as Fermi surface nesting and orbital ordering.

From this first chemical approach, we conclude that non-bonding electrons states are very unstable with respect to symmetry-breaking perturbations such as phonons. The electronic structure instantaneously adapts to the atomic oscillations to minimize the energy of the system; as quoted by Maupertuis three centuries ago: “Nature always uses the simplest means to accomplish its effects”.

The key question here is the time scale: atomic oscillations occur at the picosecond scale, while electrons visit interatomic distances at the tens of attosecond scale only. Down to which time scale can we talk about succession of states, instead of state mixing?

2.2 Sketching a chemical scenario.

We have emphasized the instability of NBE with respect to static or dynamical distortions in high-symmetry sites. A phonon mode can induce a succession of symmetry-broken and symmetry-unbroken states, with inverse local distortions at each half-period. Obviously, symmetry-broken states last much longer than intermediate high-symmetry states, along one period of vibration. Even if formally instantaneous, we will consider a very short time span δt for the symmetry-unbroken state, with respect to the period.

The period increases along with the softening of the phonon mode; for narrow bands (under-doped samples), the phonon softening with decreasing temperature leads eventually to an ordered phase, of short or long range, with the freezing of charge transfer, magnetic or orbital order, stripe or checkerboard-type structures.

For broad bands (over-doped samples), and beside the very short δt time span, the softening should lead to a metallic phase of Fermi-liquid type.

For intermediate band widths, the symmetry breaking induces a gap between the occupied electron band and the unoccupied band. A half-period later, the role of the two bands reverses along with a band crossing. The non-crossing rule (NCR, shown in Figure 2 for states as well as for COs [22]), can be retrieved if a superconducting (BCS type) gap opens, which involves the mixing of occupied (ϕ_o) and unoccupied (ϕ_u) pair states, of wave vectors (***k***, -***k***) and (***k'***, -***k'***) respectively, according to Whangbo [23]:

$$< \Phi_o(\boldsymbol{k}).\Phi_o(-\boldsymbol{k})|H'|\Phi_u(\boldsymbol{k}').\Phi_u(-\boldsymbol{k}') > \qquad [3]$$

The nucleation of the superconducting phase will be favored if pseudo-local pair states are also present at Fermi level, i.e. if the bands above cross a non-dispersive band such as those arising from carbon atomic clusters in rare earth halogeno-carbides (for example in $Y_2I_2C_2$ with T_C = 10 K [14]).

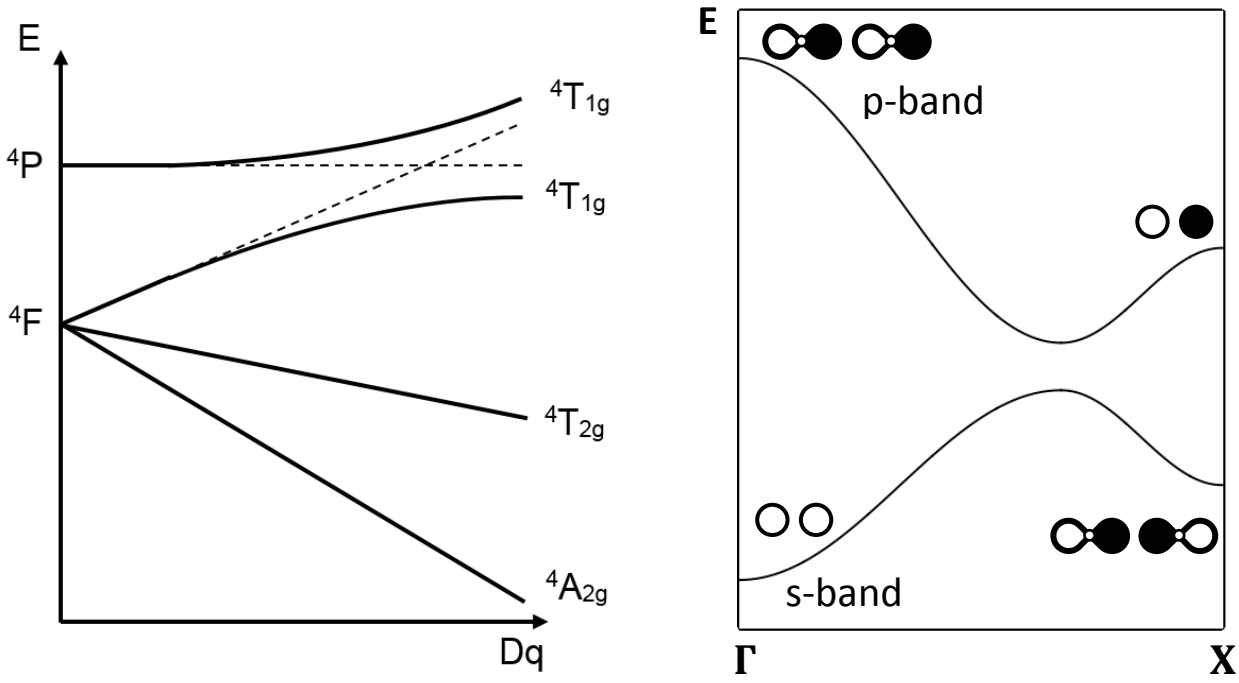

Figure 2. Schematic representations of the non-crossing rule (NCR) for state $^4T_{1g}$ (^4F, ^4P) of Cr^{3+} [22], and for a 1D band with s-p hybridization.

3. Metallic and superconducting behavior of $SrTiO_3$.

From the crystallographic point of view, $SrTiO_3$ is a perfect perovskite; its Goldschmidt factor is strictly equal to unity. When stoichiometric, $SrTiO_3$ is a dielectric insulator with a relative

permittivity rising to about 20,000 at low temperature, typical of a quantum ferroelectric. The substitution of Ca^{2+} to Sr^{2+} (few %), with different ionic radii, induces the ferroelectric instability.

On the other side, a slight non-stoichiometry due to oxygen vacancies generates n-type charge carriers and a metallic state, and even a superconducting state below 1 K, despite a very small carrier density [15]. As mentioned earlier, there might exist a link between the charge ordering in an insulating ferroelectric phase and the spin and kinetic moment ordering in a superconducting phase. Actually, materials both metallic and polar are scarce and poorly understood so far [16]. In 2017, Rischau et al showed that these two kind of order can coexist, even reinforce each other [15].

Is there a chemical explanation to those non-conventional results? In the first part, we showed how non-bonding electrons of pure oxygen character, at the top of the valence band, could become partly bonding following a tetragonal distortion of ferroelectric type in $BaTiO_3$. Conversely, pure Ti-character non-bonding states are destabilized; the band gap increases, but the stability of the compound is not affected since the conduction band is empty.

The latter argument is no longer valid if electrons are introduced by doping: their destabilization competes with the stabilization of the top of the valence band, and thus with the ferroelectric instability itself. This is observed in tungsten bronzes such as Na_xWO_3 ($0 < x < 1$), known for more than a century, in which the ferroelectric instability of WO_3 disappears progressively for x up to ca. 0.2 [24]. It is therefore understandable than superconductivity in $SrTiO_3$ remains limited in terms of electron doping rate (<0.001).

Two preliminary remarks must be done:

i) The Mott-type insulator-metal transition limits the product of the cubic root of the carrier density by the Bohr radius (corrected by the dielectric constant) a_H^* to a value close to 0.2, as illustrated by the Edwards and Sienko line [25]. When the dielectric constant is very high, a_H^* may reach values as high as the micrometer; this is precisely what occurs in $SrTiO_3$ at low temperature.

ii) The ferroelectric distortion induces a splitting of the conduction band into two bands, namely $\pi^*(e_g)$ and $\pi^*(b_{2g})$ with e_g = xz, yz and b_{2g} = xy. The two bands unfold in 3D and 2D, respectively (Figure 3).

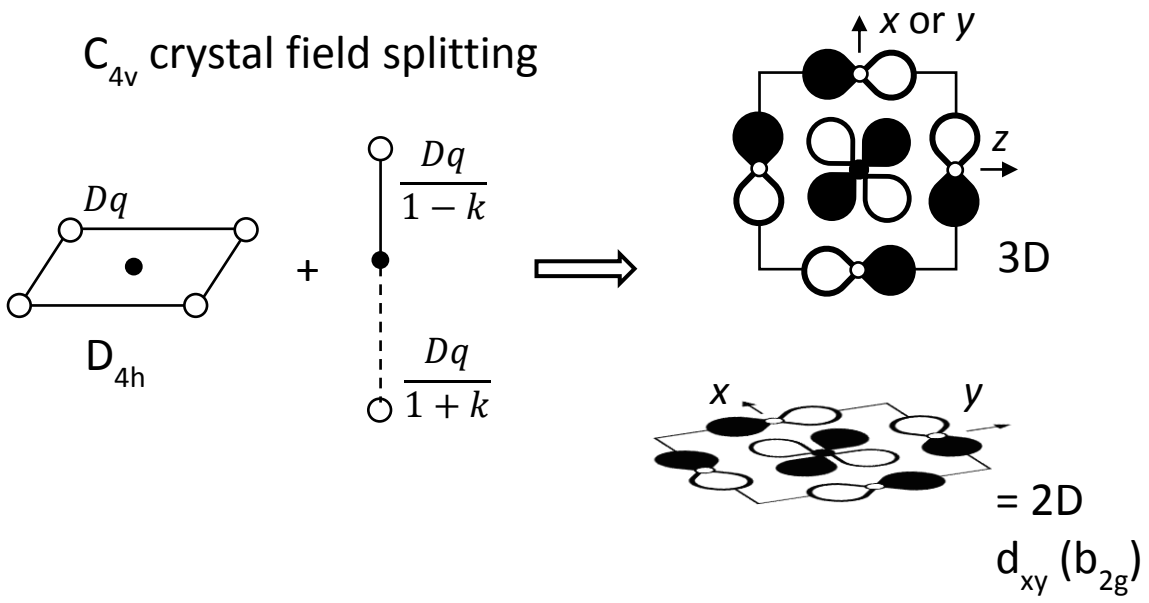

Figure 3. Crystal field splitting of t_{2g} atomic orbitals from O_h to C_{4v} symmetry, from the ligand field contributions of a non-centered axial ligand pair.

A simple crystal field approach accounts qualitatively for this band splitting, by summing the potentials in units of the *D*q phenomenological parameter used by chemists. The two axial (short and long bonds) and the four equatorial (normal bonds) Ti-O interactions are described by the potentials *D*q/(1-k), Dq/(1+k) and Dq, respectively (0<k<1). The band splitting leads to a stabilization of the b_{2g} singlet ($-6.28k^2$) with respect to the e_g doublet ($+1.14k^2$).

The first carriers then occupy the narrow 2D $\pi^*(b_{2g})$ band, with a fermionic character, but also as electron pairs of boson type, since their Coulomb repulsion on the same orbital almost vanishes ($U \approx 0$). Their coherence length should be close to the one in BCS-type superconductors such as Nb_3Sn (few hundreds nm). Under the phonon modes discussed above, those pseudo-local pairs – which are not yet proper Cooper pairs – mix, at each ¼ period, with empty t_{2g} states arising from $t_{2g} = b_{2g} + e_g$. Then, they can separate according to $b_{2g}^2 \rightarrow b_{2g}^1 + e_g^1 \rightarrow t_{2g}^2$ into a Fermi liquid, or mix with empty e_g or t_{2g} states according to b_{2g}^2 (pseudo-local pairs) + $t_{2g}^0 \rightarrow t_{2g}^{\uparrow\downarrow}$, i.e. Cooper pairs with opening of a superconducting gap.

$$< b_{2g}^1(k).\bar{b}_{2g}^1(-k)|H'|t_{2g}^0(k').\bar{t}_{2g}^0(-k') > \qquad [4]$$

In essence, the ferroelectric instability (provided by the small doping (Ca^{2+}) and due to the non-bonding character of electrons at the top of the valence band) induces a bi-stable electron system coupled to the oscillations of the axial oxygen atom. Here, we have all the ingredients for a two-band scenario, with a broad 3D-band and a narrow 2D-band; the first is constituted

of empty states, the second contains electron pairs thanks to $U \approx 0$ and a large dielectric constant. The two bands mix before the gap closure, into a superconducting state even with such low carrier densities as 10^{17} cm^{-3}.

A simple electronic Hamiltonian H' replaces here the (delayed) electron-phonon coupling Hamiltonian of the BCS model. This chemist's view applies to $SrTiO_3$-$LaAlO_3$ hetero-structures as well, justifying the intrinsic doping and the ferroelectric-type distortions expected in these structures. $SrTiO_3$ can be viewed as a succession of neutral TiO_2 and SrO layers; $LaAlO_3$, a perovskite as well, has charged AlO_2^- and LaO^+ layers. A charged interface is thus considered, with a composition $La_{0.5}Sr_{0.5}O^{+0.5}$. The electric field gradient between LaO^+ and neutral SrO layers should be screened, alike in p-n junctions, by a charge transfer : $TiO_2 + AlO_2^- \rightarrow (TiO_2)^{-\delta} + (AlO_2)^{-(1-\delta)}$, which is actually a charge transfer between O^{2-} (AlO_2) and Ti^{4+} (TiO_2); the e^-/h^+ pair opposes then the electric field gradient.

Also, the Ti-O-Al entity is dissymmetrical in terms of chemical bonding and, in the same way as a ferroelectric distortion, induces both a band splitting from t_{2g}* into b_{2g}*+ e_g* and a dynamical polarization of TiO_2 layers away from the interface. Therefore, the first non-bonding electrons in the conduction band (t_{2g}*) will undergo a succession of quasi-local pair states ($b_{2g}^{\uparrow\downarrow}$, few hundreds nm) and delocalized Cooper-pair states, thanks to the mixing with empty e_g or t_{2g} states when the gap closes. Such a description is close to that of Gariglio et al. [26] in their review on interface superconductivity.

4. High-T_C superconducting cuprates.

A significant difference between cuprates and titanates is the one-electron energy (Coulomb integral) for 3d orbitals. Ti and Cu 3d states lie respectively above and below O 2p orbitals, which affects the electronic structure: in cuprates with optimum doping, the valence band should be of dominant Cu-character, the conduction band being mostly of oxygen character.

La_2CuO_4, structural parent of superconducting cuprates, is a charge transfer insulator with a first excited state described by $O^{2-} + Cu^{2+} \rightarrow O^- + Cu^+$. It is also an antiferromagnet with a Neel temperature close to ambient. La_2CuO_4 is most of the time p-doped by substitution of Ba^{2+} or Sr^{2+} to La^{3+}, or by chemical or electrochemical intercalation of oxygen in La_2O_2 rock salt-type layers. 8 to 20 % doping rates induce a metallic then superconducting state ($T_C \approx 40$ K), along

with a significant decrease of the unit cell volume; shortened interatomic distances lead to larger $t_{Cu\text{-}O}$ transfer integrals and thus to larger band widths, but also to stronger oxygen-oxygen interactions that turn out to be of major relevance here.

Along with doping, band widths increase and the value of the Hubbard parameter decreases due to covalency (*U* is related to Racah repulsion parameters *B* and *C*, familiar to chemists, and sensitive to covalency); this is consistent with an insulator-metal transition of Mott-Hubbard type, for increasing *t*/*U* ratio.

We start from this framework, with $U \approx 0$, to describe the electronic structure of cuprates with optimum doping (i.e. formally $Cu^{(2+x)+}$ with x close to 0.15). $U \approx 0$ means a full $O^{2-} + Cu^{2+} \rightarrow O^{-} + Cu^{+}$ transfer, Cu^{+}/O^{-} being the ground state. This is justified by several arguments:

i) Coulomb integral values, $H_{dd}(Cu)$ =-18.7 eV and $H_{pp}(O)$ = -17.1 eV [27]. Tight-binding calculations for $(CuO_4)^{5-}$ square planar clusters, such as found in $La_2Li_{0.5}Cu_{0.5}O_4$ [28], show clearly this charge transfer situation (Figure 4 in Ref. 29).

ii) Doping holes in cuprates are essentially located on oxygen atoms, as demonstrated by the pioneering works of Bianconi et al. [30] by X-ray absorption spectroscopy (XANES), later on by electron-loss spectroscopy (EELS) [31] and by spectacular atomic scale imaging from tunneling asymmetry, even on underdoped samples, by Hanaguri et al. [32], Kohsaka et al. [33], or Pasupathy et al. [34], showing inhomogeneous charge distributions as nano-scale stripes or checkerboard patterns on oxygen atoms.

iii) Recent works by Jurkutat et al. [35] using NMR on $^{63\text{-}65}Cu$ and ^{17}O doped samples, leading to a phase diagram for T_C as a function of the distribution of doping holes at Cu and O sites.

4.1 $(CuO_2)^{2-}$ unit cell.

The input data for our tight-binding calculations are reported in Table 1. Figure 4 shows the dispersion curves $E(\boldsymbol{k})$ in the -19 to -15 eV range.

Figure 5 shows an enlarged view of the two top bands, between -17 and -15 eV, noted here $\sigma^*(b_{1g})$ and $\pi^*(a_{2g})$ (as referred to the point symmetry of the copper site, at the M1 point of BZ1). At Γ, these two bands are degenerate and of pure oxygen character (Figure 5a). The top

band, $\sigma^*(b_{1g})$, is broad ($W \approx 1.5$ eV) due to strong Cu-O and O-O antibonding interactions; the $\pi^*(a_{2g})$ band is narrow ($W \approx 0.3$ eV) because of its Cu-O non-bonding character (especially in Γ, M1) or by compensation of Cu-O and O-O antibonding/bonding interactions (in X1).

Several bands are identified:

i) Around -19 eV, a valence band of Cu character and Cu-O bonding interactions,

ii) Between -18 and -15 eV, a broad conduction band of oxygen character, and Cu-O generally antibonding,

The $E(\boldsymbol{k})$ curve for $\sigma^*(b_{1g})$ shows a saddle point in X1, associated to a van Hove-type peak in the density of states (this point will be discussed later). The corresponding crystal orbital has contributions from Cu 4s, z^2 and x^2-y^2 with respective weights of 0.037, 0.088 and 0.252. The 4s-z^2 hybridization is well known for the Jahn-Teller Cu^{2+} ion. The other contribution is from the $2p_x$ orbital of one oxygen, with a weight of 0.650. Thus, the oxygen character is approximately twice the copper character in this crystal orbital, and the bonding is strongly anisotropic with large antibonding interactions along [100] and non-bonding interactions along [010] (Figure 5e). This non-bonding character in X1 offers the possibility of opening a static or dynamical gap of nematic type ($a \neq b$), with the creation of a double-well potential as in $SrTiO_3$. For the Fermi level to be located in X1 for the $\sigma^*(b_{1g})$ band, a hole doping rate of 12-15% should be necessary. This approach, which agrees with experiment, does not discriminate electrons and doping holes; doping is used to shift the Fermi level toward a high-symmetry point of the Brillouin zone.

Table1. Parameters for Extended Hückel tight-binding calculations: H_{ii}'s are the diagonal matrix elements of the effective Hamiltonian, ζ_i's and c_i's are respectively the exponents and contraction coefficients for the Slater-type AOs.

Element	AO	H_{ii} (eV)	ζ_1	c_1	ζ_2	c_2
Cu	4s	-7.44	2.151	0.48071	1.168	0.61474
	4p	-4.26	1.370	1.0		
	3d	-18.7	7.025	0.44221	3.004	0.68886
O	2s	-33.7	2.246	1.0		
	2p	-17.1	2.227	1.0		
Fe	4s	-9.1	1.900	1.0		
	4p	-5.32	1.900	1.0		
	3d	-12.6	5.350	0.55050	2.000	0.62600
Se	4s	-20.5	2.440	1.0		
	4p	-13.2	2.070	1.0		

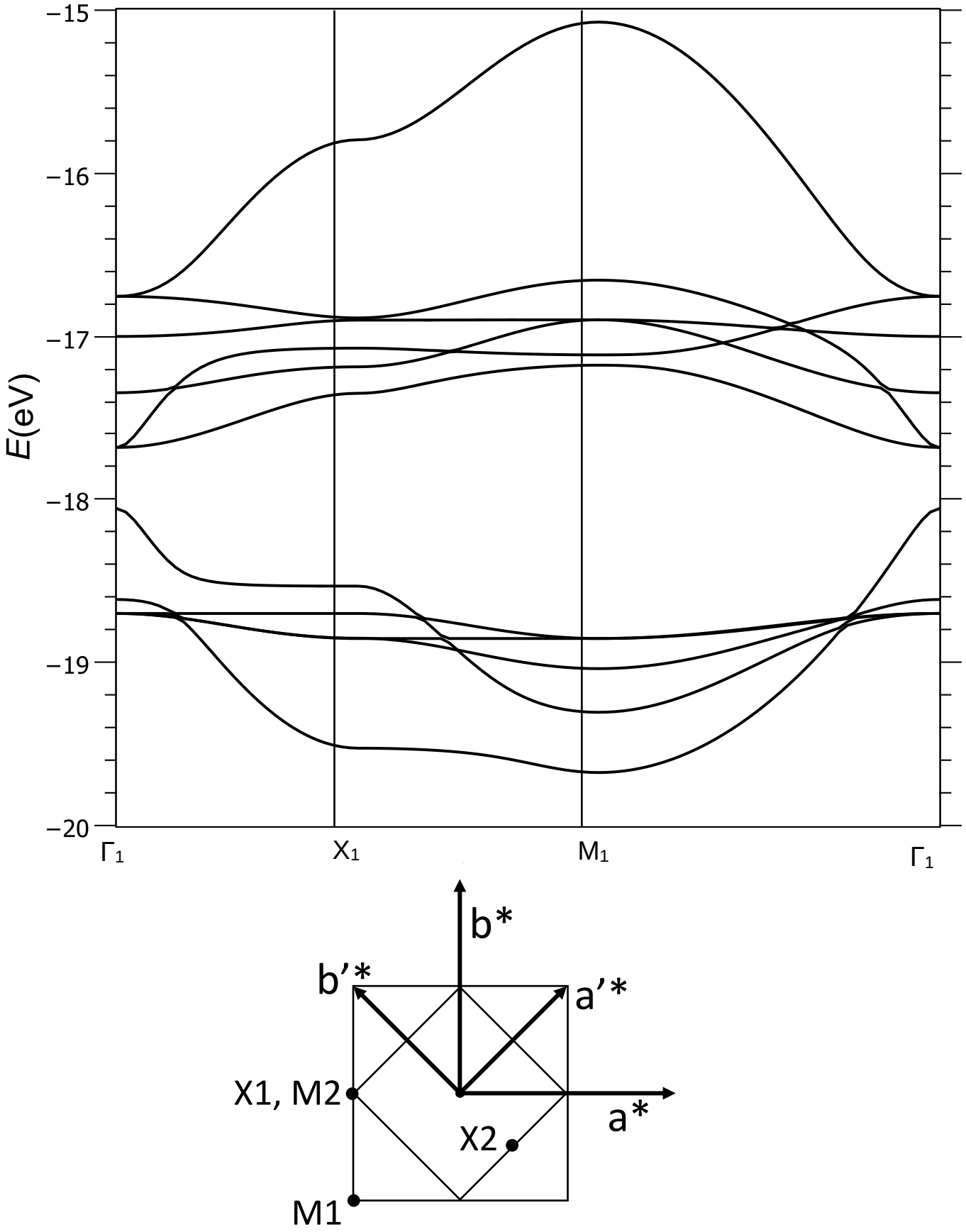

Figure 4. Top: dispersion curves $E(\boldsymbol{k})$ for a $(CuO_2)^{2-}$ unit cell, from tight-binding calculations. Bottom: Brillouin zones for the single and double unit cells (BZ1 and BZ2), and their high symmetry points.

4.2. The double unit cell $(Cu_2O_4)^{4-}$.

Figure 5a shows the same dispersion curves $E(\boldsymbol{k})$ for a double unit cell $(Cu_2O_4)^{4-}$ but with a different CO's distribution in the both sites. The hybridization of z^2 and x^2-y^2 reinforces the anisotropy of the (anti)bonding between copper and oxygen (Figure 5e). Besides, we can consider the hypothesis of a distribution of those two orbitals over two distinct sites (orbital ordering).

The correspondence between the Brillouin zones and high symmetry k-points of the single (BZ1, M1, X1…) and double unit cell (BZ2, $\Gamma 2$, M2…) is shown in Figure 4b.

The M2 point, corresponding to X1 for the single unit cell, shows a degeneracy between an energy band arising from σ*(b_{1g}) (M1 corresponds to $\Gamma 2$) and a lower energy band arising from $2e_u$ ($\Gamma 1$) (Figure 5a). Both bands show a full and opposite orbital ordering on copper sites labelled (1) and (2) (Figure 5d), and appear isotropic since the weights on oxygen atoms are identical. The symmetries on the two copper sites are different: a_{1g} and b_{1g}, which confirms the proposed 1:1 orbital ordering. Each oxygen atom, overall non-bonding, becomes a Janus entity, bonding on one side (with respect to a_{1g} O-O bonding) and Cu-O antibonding on both sides, but weakly in a_{1g} (c_i^2=0.15), stronger in b_{1g} (c_i^2=0.22), thus fully non-symmetric. Compared to X1 (spatially dissymmetric, antibonding/bonding along [100] and non-bonding along [010] (Figure 5e), with the reverse situation at Y1), M2 doesn't show any tendency to nematicity, but rather a strong tendency to the coupling to an optical mode of breathing type, with a dynamical inversion of copper sites (1) and (2) (Peierls-type 2D instability); a tight-binding calculation (EHTB) leads to a gap opening of 33 meV per pm of phonon amplitude.

We have here too a critical hypothesis, with an oscillating band gap driven by a phonon mode. At each half-period, the two bands cross; at this very moment, the non-crossing rule suggests the opening of an electronic gap, followed by a superconducting gap $2\Delta_{SC}$ by mixing the two bands according to:

$$< e_u^1(\boldsymbol{k}).\bar{e}_u^1(-\boldsymbol{k})|H'|b_{1g}^0(\boldsymbol{k}').\bar{b}_{1g}^0(-\boldsymbol{k}') > \qquad [5]$$

Figure 6a shows the evolution of the ground state along a phonon half-period (-π/2 to +π/2), from a b_{1g} (resp. a_{1g}) enlarged (resp. compressed) site, as a function of the oxygen displacement δ. Two types of domains can be observed: i) on both sides, a smooth evolution of the e_u and b_1 band edges with δ; ii) in the middle, a progressive mixing of e_u and b_1, up to a full reversal. Figure 6b represents the COs before and after mixing for a 50:50 ratio.

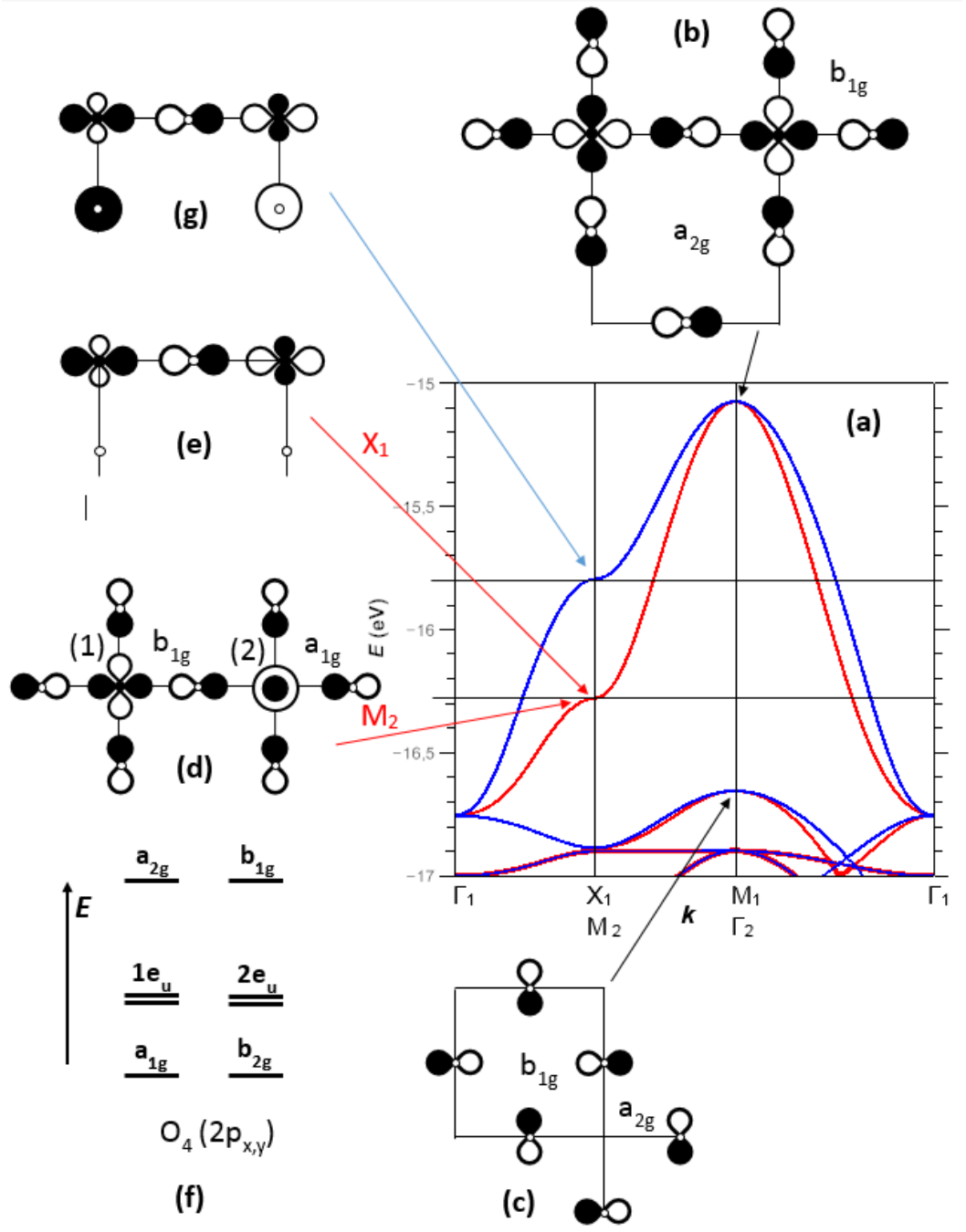

Figure 5. (a) Enlarged view of the two upper σ*(b_{1g}) and π*(a_{2g}) bands of Figure 4 with (blue) and without (red) participation of oxygen 2s AOs. Representations of COs belonging to single and double unit cells (indexed 1 and 2, respectively): (b) σ*(b_{1g}) CO in M1(Γ2) with b_{1g} and a_{2g} symmetries for the copper occupied and non-occupied sites, respectively. (c) π*(a_{2g}) CO in M1, with a_{2g} and b_{1g} symmetries for the copper occupied and non-occupied sites, respectively. (d) CO at the saddle point in M2, with two different copper sites of b_{1g} (1) and a_{1g} (2) symmetry; in the middle, oxygen lies in a strongly asymmetric environment - a Janus atom-, with a large 2p-(x^2-y^2) overlap vs. a small 2p-z^2 overlap; O-O interactions are antibonding around b_{1g} and bonding around a_{1g}. (e) CO with same anisotropy in X1 than (d), but not leading to 1:1 orbital ordering (O-O), by differentiating [100] from [010]

directions. (f) Eight molecular orbitals for a square O_4 group, considering $2p_x$ and $2p_y$ only. (g) Role of oxygen 2s orbitals, decreasing the anisotropy found in (e).

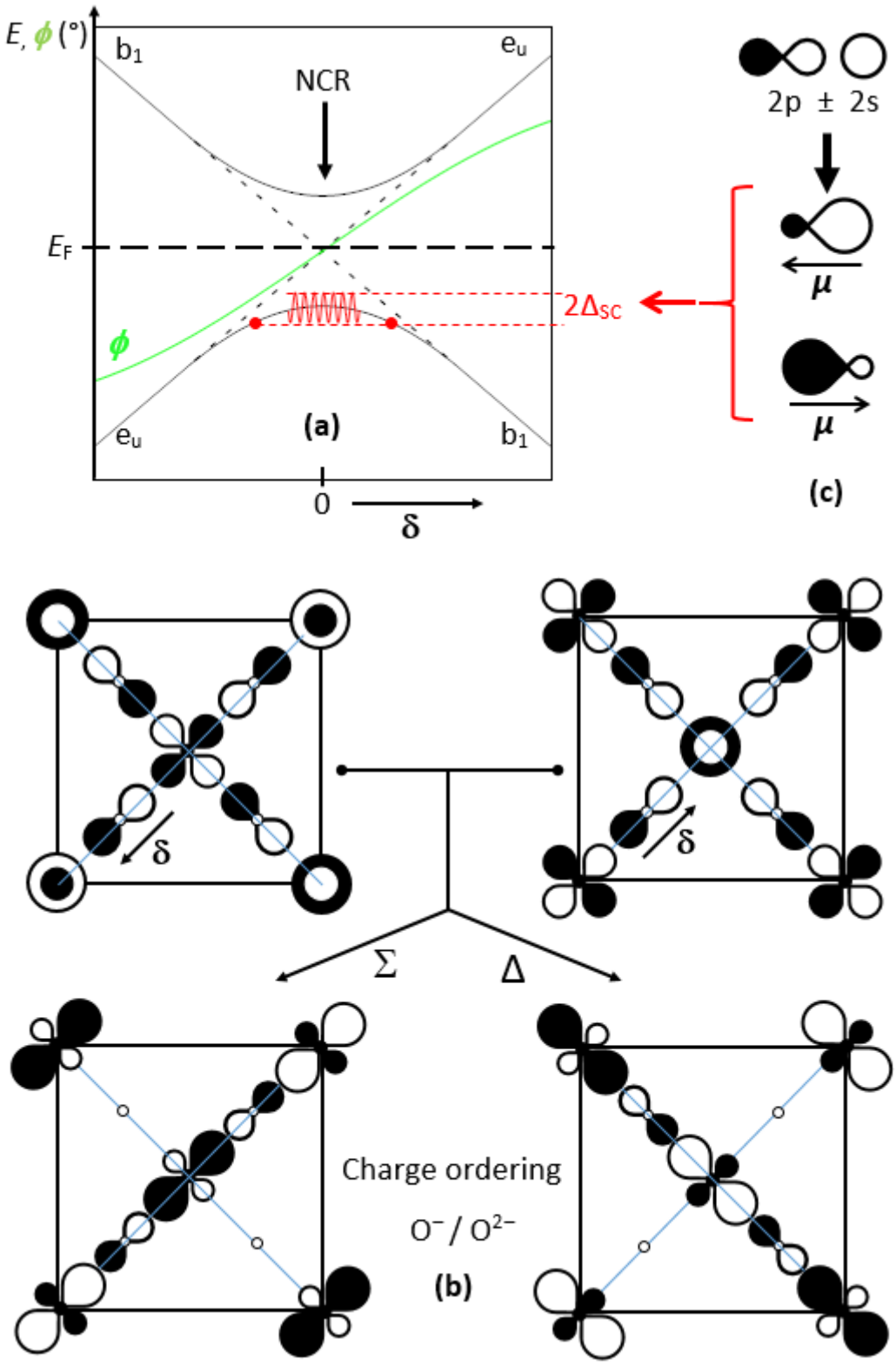

Figure 6. (a) Effect of the NCR along the phonon ϕ of amplitude δ. On the left side, the occupied e_u band with large b_{1g} and small a_{1g} sites. On the right side, the same sites but for inverse δ and for the occupied b_1 band. (b) Mixing the two bands at 50/50 and δ = 0 evens the copper charges and conversely differentiates strongly two among four oxygen atoms, inducing charge fluctuations. Hole doping

creates $(O_4)^{5-}$ that should disproportionate into $(O_4)^{6-}$ and $(O_4)^{4-}$. (c) Oxygen dipole reversal induced by 2s-2p hybridization and ϕ.

The hybridization of x^2-y^2 and z^2 favors one direction over [100] and (010], as observed above in X1, and evens the weights on both copper ions; conversely, it strongly discriminates the four oxygen atoms, two of them having then vanishing CO coefficients. However, and as we will discuss later, this charge ordering partially disappears by delocalization of the two holes among an $(O_4)^{6-}$ cluster. From the above it can be retained that such CO mixing leads to CT through electron (hole) pairs.

Another important feature is the high polarizability of O^{2-}, whose electronic dipole (due to its Janus character) may oscillate at high frequency, a few orders of magnitude faster than phonons. Such a behavior can be considered as the result of O(2p)/O(2s) AOs hybridization (Figure 6c). This dipole oscillation may contribute, alike in atomic spinodes, to induce a decomposition into various components of the e_u/b_1 mixtures in equilibrium, exchanging hole pairs, and consequently leading to the Whangbo Hamiltonian of pair-occupied and non-occupied states.

4.3. The $\pi^*(a_{2g})$ band.

As proposed in 1990 by Micnas et al. and later illustrated by Simon [13,14], the crossing of a broad and a narrow band close to Fermi level would be a key factor for the coupling of quasi-local pairs (narrow band) and fermions (broad band), to form Cooper pairs.

Could the narrow, 300 meV-wide $\pi^*(a_{2g})$ band be shifted to Fermi level (it lies approximately 400 meV below it) and generate local electron pairs? For this band, Figure 7 illustrates: i) in X1(M2): the a_{2g}- b_{2g} orbital ordering, overall O-O non-bonding character and Cu-O antibonding character at the b_{2g} site; ii) in M1: the a_{2g} symmetry of each copper site, for which oxygen atomic orbitals show b_{1g}-type overlap on vacant cationic sites (½ ½ 0) with antibonding O-O character identical to the $\sigma^*(b_{1g})$ band for copper (see also Figure 5c).

4.3.1. Positioning of the $\pi^*(a_{2g})$ band.

The $(CuO_2)^{2-}$ layer is sandwiched between so-called reservoir layers, in which the doping allows adjusting the rate of charge carriers in the CuO_2 layer. Also, being ionic, these reservoir layers generate an electrostatic (Madelung) potential that can be estimated by the Ewald summation method. One has to consider as well the screening of the Madelung potential by the charge

carriers of the conducting layer; therefore, we restrict the calculation of Madelung potentials to the contribution of a few neighbor cells, and consider orders of magnitude only.

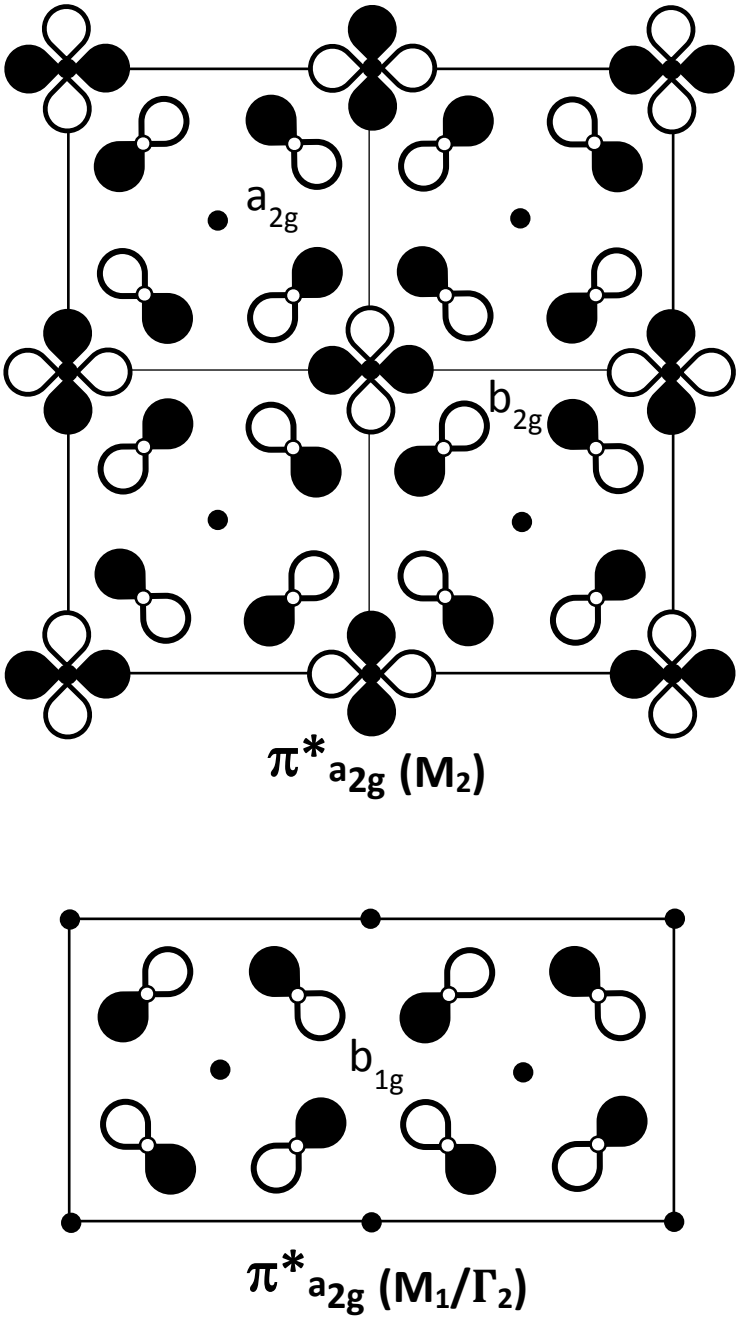

Figure 7. Crystal orbitals of the narrow $\pi^*(a_{2g})$ bands at X1 (M2) and M1 points of the BZ.

It is also straightforward to compare the importance of the Cu-O charge transfer in CuO2 layers, by considering three cases in Madelung terms: Cu^{2+}/O^{2-}, $Cu^{+}/O^{1.5-}$ and Cu^{0}/O^{-}. A few comments arise from these rough calculations: i) as expected, the potential at the copper site is negative, whatever the Cu-O charge transfer case; ii) the potential at the oxygen site is

positive, except for the non-significant Cu^0/O^- case; iii) at the vacant cationic site (½ ½ 0, that will be labelled (+) in the following), the Madelung potential $V_M(+)$ is negative whatever the charge transfer case, but lower by ca. 1/3 than the potential at the occupied site, in absolute value. This justifies a specific treatment for the antibonding electrons in the $\pi^*(a_{2g})$ band; iv) the negative character of the $V_M(+)$ potential increases when the apical Cu-O distance (i.e., the separation between the CuO_2 and the reservoir layer) increases.

Therefore, the negative Madelung potential reinforces the destabilization of electrons at the vacant cationic site, adding up to the antibonding character of O-O interactions. These features should favor the stabilization of doping holes near the vacant (½ ½ 0) cationic sites of the CuO_2 layer. How many holes? Can we envisage a hole pair on oxygen entities as well known for electrons and in b_{2g} of electron doped $SrTiO_3$, i.e. a dimerization $(O_4)^{5-} + (O_4)^{5-} \rightarrow (O_4)^{4-} + (O_4)^{6-}$? We would then obtain what chemists would call *a hole lone pair*, or an *antiatom* with a pseudo negative nucleus arising from $V_M(+) \leq 0$; the two holes would then have a wave function of x^2-y^2 type, of b_{1g} symmetry.

4.3.2. Mulliken-Jaffé electronegativity for oxygen.

In M1, $\pi^*(a_{2g})$ is of pure oxygen character. We can express the energy $E(q)$ of the oxygen ion as a function of its charge q, its electronic affinity $EA(q)$ and its ionization potential $IE(q)$:

$$E(q) = \alpha.q + \beta.q^2 + \gamma.q^3 \qquad [6]$$

where $\alpha = \frac{1}{2}.\big(IE(q) - EA(q)\big)$ is the Mulliken electronegativity, β is Pearson's hardness and γ is an adjustable parameter; for oxygen, α = 6.925, β = 6.190 and γ = 0.505. $E(q)$ is plotted on Figure 8.

The Mulliken-Jaffé electronegativity χ_{MJ} is defined as the derivative of $E(q)$ with respect to q. As seen on Figure 8, χ_{MJ} vanishes for $q \approx -0.6$ and is negative below this q value. Also, it shows that O^{2-} is not stable in gaseous phase, and will likely lose an electron at the surface of an oxide - catalysts take advantage of this effect-.

Therefore, to account for the electronegativity of oxygen in an iono-covalent lattice, it is necessary to add a Madelung-type term in Eq° 6. The magnitude of this term is difficult to estimate, since oxygen outer electrons lie away from the exact site position. Since the Madelung energy is proportional to q^2, we will use the corrected expression

$$E(q) = \alpha.q + (\beta - k').q^2 + \gamma.q^3 \qquad [7]$$

for the energy of the oxygen ion as a function of its charge *q*. Figure 8 illustrates the importance of this Madelung term: i) the minima are displaced toward the most negative charges (most ionic configurations), ii) *E*(*q*) curves flatten, around their minima, until *k'* = 2.8. If we start from the $(O_4)^{8-}$ cluster, oxidized into $(O_4)^{6-}$ by charge transfer, at the X-point of the BZ, its progressive oxidation by doping into $(O_4)^{5-}$ then $(O_4)^{4-}$ corresponds to a maximum 0.5 electron per oxygen, for example between O^{-1} and $O^{-1.5}$ which formation energies *E*(*q*=-1.0) and *E*(*q*=-1.5) do not differ by more than 50 meV (Figure 8). This energy difference is less than the O-O resonance energy, which can be estimated to a hundred meV approximately (Figure 4 of Ref. 29); this leads to *U*<0, as in the negative-*U* model for superconductivity [36].

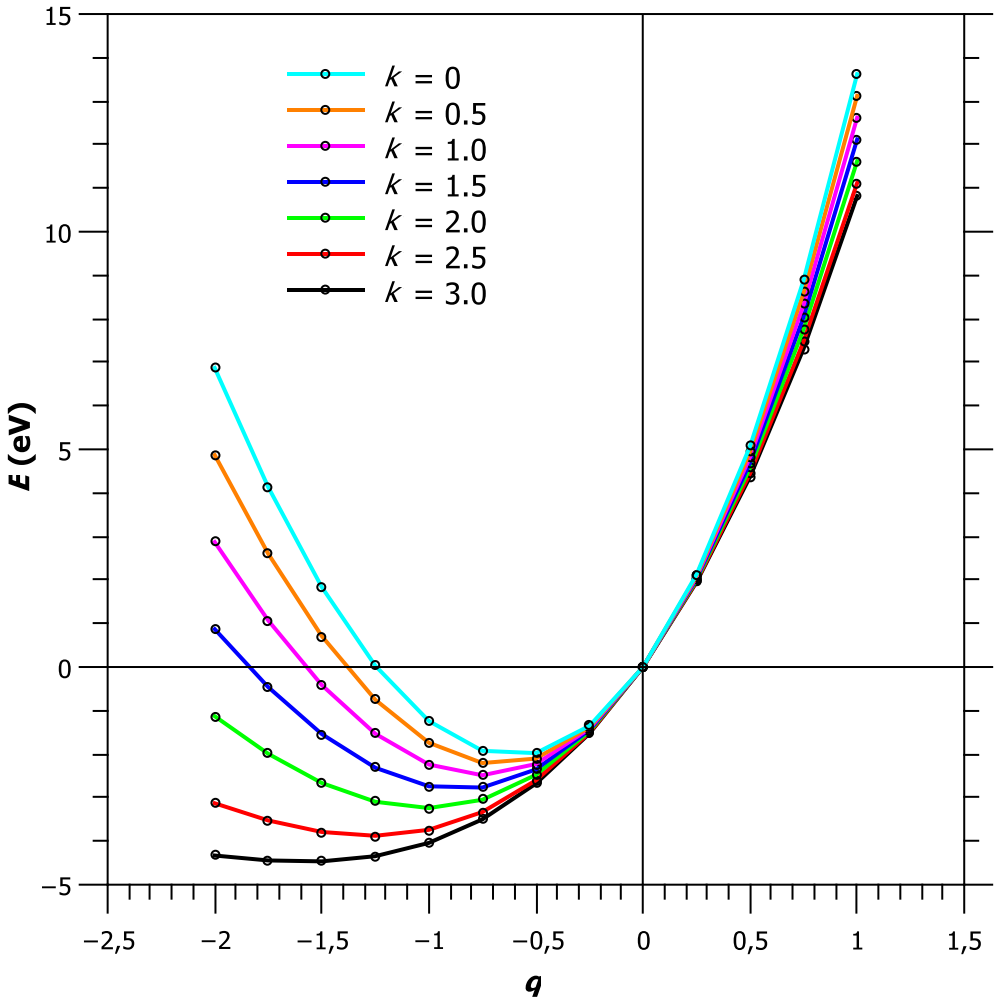

Figure 8. Formation energy *E*(*q*) of an O^q ion (-2 < q < 1), related to the Mulliken-Jaffe electronegativity $\chi_{M\text{-}J}$, for the free ion (k' = 0) as well as for an ion embedded in a Madelung potential (k'≠ 0).

In conclusion from above chapters, we can describe the electronic structure of $(CuO_2)^{2-}$ layers by a network of O_4 square-planar entities (Figure 9), corresponding to the four molecular

orbitals b_{1g}, a_{2g}, $1e_u$, $2e_u$, a_{1g} and b_{2g} (Figure 5f), neglecting out-of plane $2p_z$ orbitals, in order of decreasing energy. In this network, cationic sites are either i) fully occupied by Cu^{2+} ions, in the tetragonal epitaxial form of t-CuO, ii) half-occupied by Cu^{2+} in high-T_C cuprate layers, iii) one-fourth occupied by Cu and one-fourth by Li^+, in an ordered manner, in insulating La_4LiCuO_8 than can be described as $(Li^+)(Cu^+)(O_4)^{6-}$ layers (*I4/mmm*), with two holes in the $\sigma^*(b_{1g})$ molecular orbital centered on each Cu^+ ion. At low *T*, this phase undergoes an orthorhombic distortion (*Ammm*), from D_{4h} to D_{2h} for Cu+ and Li^+ ions, with a buckling of distorted sites.

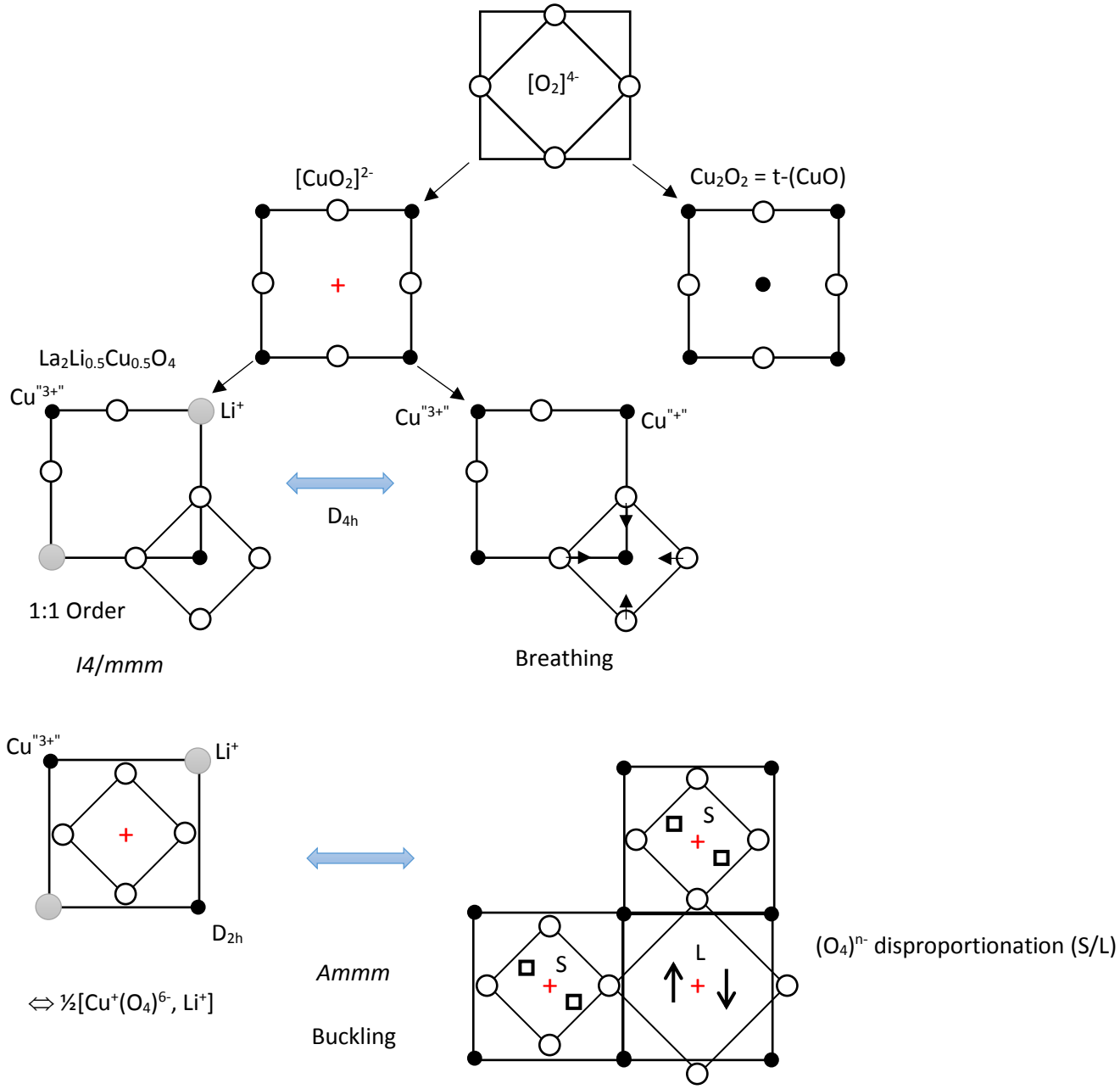

Figure 9. $((Cu,Li)O_2)^{2-}$ layers built from $(O_4)^{n-}$ square planar entities, with ordering or buckling, illustrating CT as well as charge disproportionation (CD) possibilities (S: small and L: large) represent such a case for $(O_4)^{5-}$ groups).

Besides, the buckling of square-planar entities splits the non-occupied cationic sites (+) into two types of sites of same D_4 symmetry but different size (labelled hereafter L and S). This atomic distortion and the increase of antibonding at S is reinforced by a 2p-2s oxygen orbitals hybridization towards S site.

These two situations can be transposed to the distortions of the O_4 network of the $(Cu_2O_4)^{4-}$ layer, with a breathing mode (arrows in Figure 9) but also a "hole disproportionation" and octahedra buckling ($2a_{2g}^1 \rightarrow a_{2g}^0 + a_{2g}^2$); this $\pi^*(a_{2g})$ band, already narrow (ca. 300 meV) and further splitted by phonons, should serve as a seed for Cooper pairs delocalized in the broad $\sigma^*(2e_u)$ band of the superconducting phase. This hole-acceptor character of $\pi^*(a_{2g})$ agrees with the statement of Hirsh et al. for locating the cuprate holes preferentially in the oxygen $2p_\pi^*$ bands [37].

4.3.3. Role of oxygen 2s atomic orbitals.

So far in this discussion, we did not consider the semi-core (or rather deep-valence) 2s orbitals of oxygen; by introducing them in the tight-binding calculations, we notice that the energy at X1 is shifted upward by ca. 500 meV (blue line in Figure 5a) due to z^2(Cu)-2s(O) antibonding interactions along [010] (Figure 5g).

Such a 2s$\pm$2p hybridization modifies the electron density in the vicinity of the oxygen ion, increasing the Cu-O antibonding character of the band in an asymmetric way and contributing significantly to the Janus effect. In an axially distorted (a_{1g}) Cu_2O_4 cell, for example, the 2s$\pm$2p hybridization reinforces the strong antibonding interactions with x^2-y^2, while it weakens the already smaller antibonding interactions with the equatorial lobe of d_{z2} orbitals. Overall, this favors the charge transfer from oxygen to copper.

Similarly, for the *Ammm* transverse distortion, the 2s$\pm$2p hybridization reinforces the strong antibonding O-O interactions in the small (S) square-planar O_4 groups, while weakening them in the large (L) ones. This favors the introduction of doping holes in this region of cationic type (negative value of the Madelung potential V_M), even their pairing.

Also, a much smaller hole density is necessary to reach the X1 point; it actually corresponds to a slight electron-doping (as in n-type cuprates). The contribution of 2s orbitals will be modulated by the competing oxygen-rare earth bonding. The important role of oxygen 2s orbitals had already been mentioned many years ago with respect to the gap value for the parent insulating phase [38]

4.4 Underdoped cuprates.

The phase diagram is complex (pseudo-gap, charge density waves, stripes, checkerboard patterns…); however, those phases should be related to characteristics of the pristine La_2CuO_4 phase. La_2CuO_4 is an insulating antiferromagnet of Mott or rather charge-transfer type, in which the lowest excitation involves the gap between the oxygen-character band and the upper Hubbard band: $O^{2-} + Cu^{2+} \rightarrow O^{-} + Cu^{+}$. This transfer can be symmetric, but limited the lone antiferromagnetic (AFM) coupling by super-exchange. We will examine the non-symmetric transfer only, which involves two copper ions (labelled 1 and 2) according to:

$\uparrow Cu(1)^{2+} + O^{2-} + \downarrow Cu(2)^{2+} \rightarrow Cu(1)^{+} + \uparrow O^{-} + \downarrow Cu(2)^{2+}$ (U) [8]

Or,

$\uparrow Cu(1)^{2+} + O^{2-} + \downarrow Cu(2)^{2+} \rightarrow \uparrow Cu(1)^{2+} + \downarrow O^{-} + Cu(2)^{+}$ (D) [9]

Where the arrows indicate the spin orientation. The remaining spin on oxygen couples with the spin ½ on Cu(2), in a bonding state in Eq° 8, in the same way as the Zhang and Rice singlet (ZRS) description [39] in the well-known *t-J* model. This will be noted CT-ZRS(U) or (D), by reference to the remaining spin of the oxygen ion. This transfer breaks the C_2 symmetry of oxygen, Cu^{+} being larger than Cu^{2+} associated to O^{-}. Thus, we can imagine a local two-dimensional 1:1 order (CT-ZRS(D)/(U): abscissa in Figure 10), possibly static but that can be coupled to a phonon mode.

Three remarks arise:

i) the charge transfer rate is formally 50% (i.e. half the optimal doping value),

ii) one magnetic network over two must disappear at each phonon half-period; this scheme is consistent with the sharp decrease of Neel temperature with doping,

iii) local ordering domains appear (U or D), separated by antiphase boundaries, and alternating at each half-period.

Figure 10 (bottom) illustrates these two situations. What is the role of doping? At each half-period, when the symmetry is not broken, doping holes can form as much ZRS-[u] than ZRS-[d] (y-axis in Figure 10). However, the formation of CT-ZRS (either D or U) at each quarter-period, on each side of the antiphase boundary, is only compatible with doping holes of the

opposite norm (d/U or u/D), thereby rejecting doping holes of the same norm (d/D or u/U) toward the other domain.

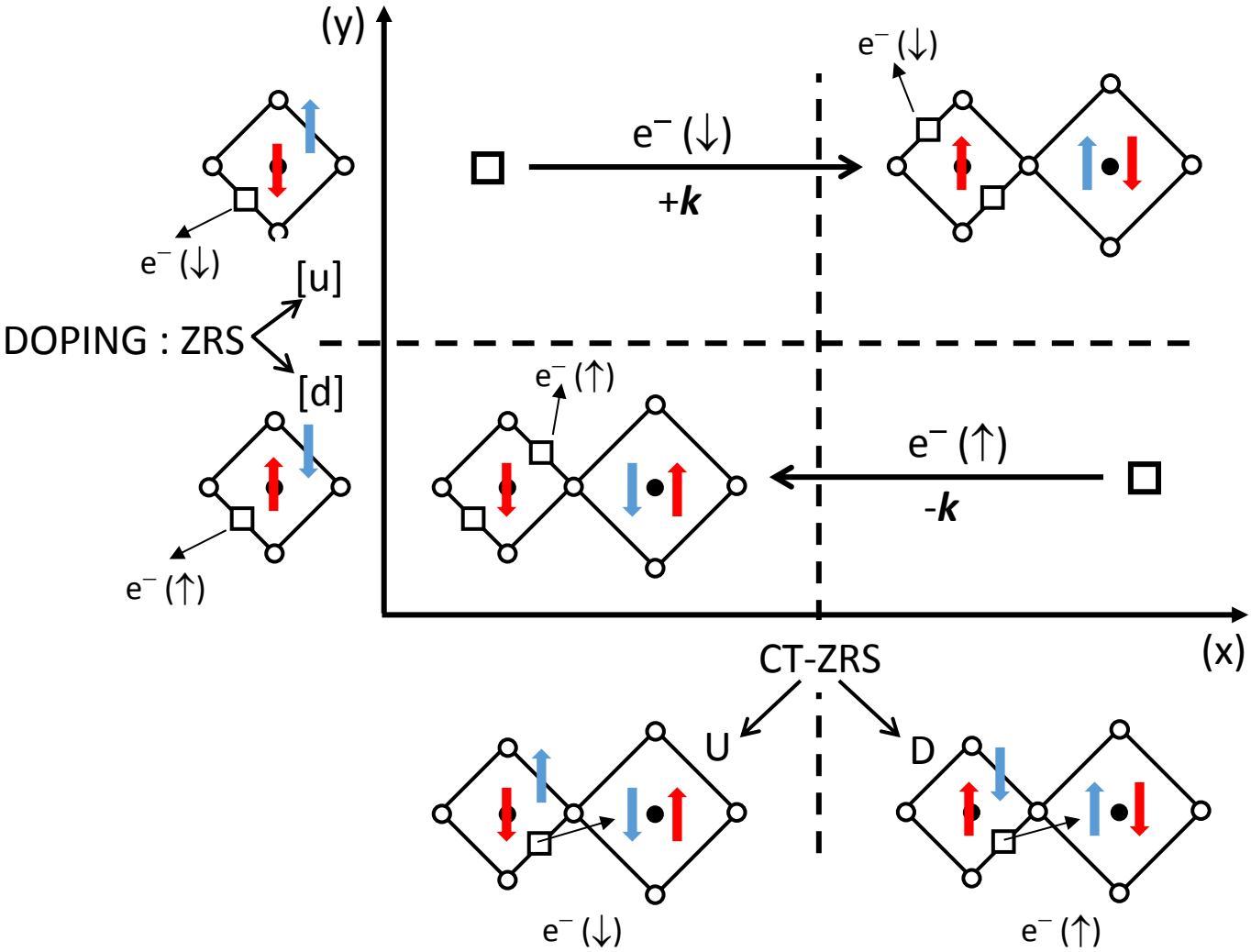

Figure 10. Phase diagram for a non-symmetric CT in under-doped cuprates, as a function of hole doping (represented as usual by a Zhang-Rice singlet (ZRS), [39], and denoted [u] or [d] according to the remaining oxygen spin) and CT between two copper atoms (denoted U and D as previously). The diagram shows avoided areas, from which some doping holes (u/U or d/D) are expelled toward another CT-type part of the crystal, giving rise to hole transfer of opposite spin and momentum (Cooper pairs).

In essence, this is a collective displacement of holes of opposite spins (u vs. d) in opposite directions (+***k*** vs. –***k***), i.e. characteristic of Cooper pairs for a possible superconducting state. Note that this mechanism leads to a density of pairs that is half the expected density, as seen experimentally [40].

In conclusion, this model agrees with the description by Reznick [41] titled “Electron-phonon coupling reflecting dynamic charge inhomogeneity in oxide superconductors”, invoking strong

bond stretching phonon anomalies common to stripe-ordered and superconducting materials, between ordered magnetic and hole-free layers, and charge transferred Cu^{+} and hole-rich oxygen ones.

5. Iron arsenides and selenides.

As soon as 1965, E. Bertaut reported the anomalous non-magnetic behavior of FeS, a rare mineral of mackinawite type, first identified in 1962 [42]. Due to its low thermal stability, FeS is difficult to obtain as a pure phase (i.e. without metallic iron as impurity). Besides, not long after the discovery of high-T_C superconductivity in the doped pnictide $LaO_{1-x}F_xFeAs$ (T_C = 26 K) by Hosono et al. in 2008 [43], the selenide β-FeSe showed superconductivity below c.a. 10 K. FeSe has the same mackinawite (*P4*/*nmm*) structure than FeS but is more stable. Furthermore, T_C in FeSe can reach 30 K either under pressure or upon S-Se substitution; both conditions correspond to a negative variation of unit cell volume, as often observed for the spin transition S = 2 → S = 0 in ferrous materials [44].

We choose to apply our tight-binding approach to FeSe, to check if similar features arise in the case of chalcogenides, compared to the same approach on titanates and cuprates. The tight-binding parameters for Fe and Se are listed in Table 1. The values of Coulomb integrals for Fe 3d and Se 4p orbitals lie within 0.6 eV, indicating a strong covalency for Fe-Se bonds. This justifies to use a vanishing (U = 0) Hubbard parameter for electron-electron repulsion,

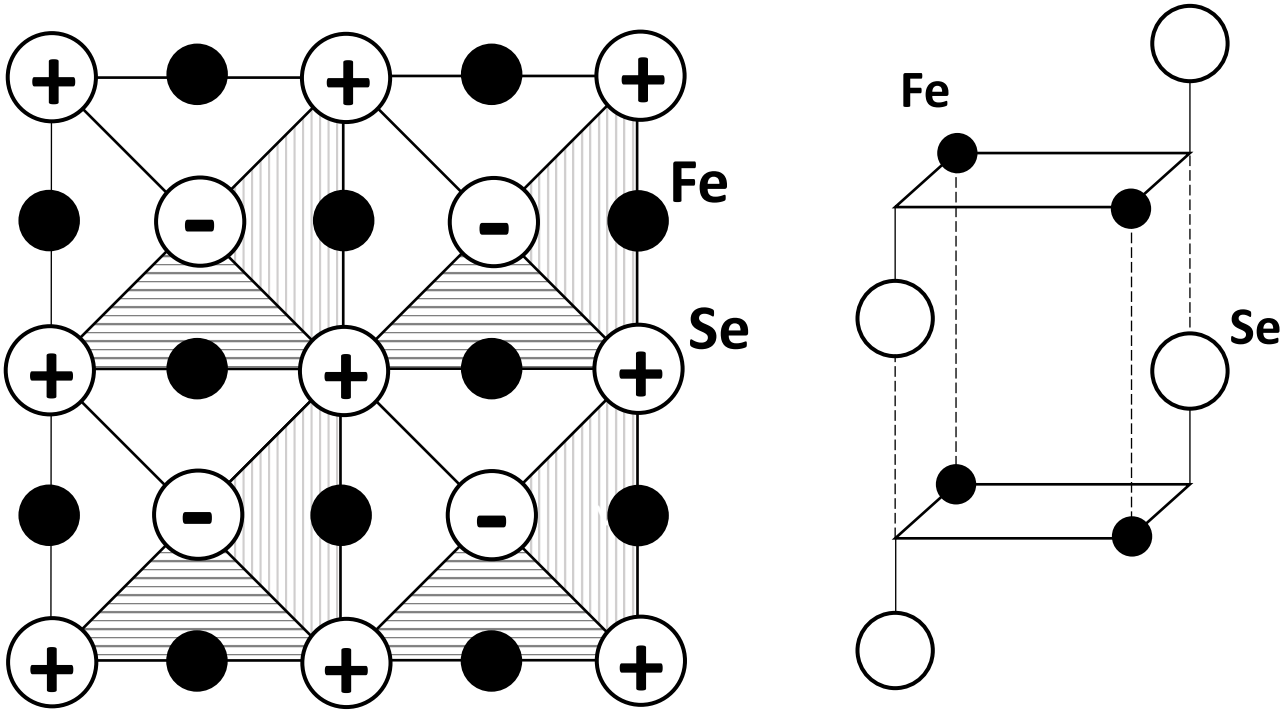

although a non-zero *U* value would have to be considered for crystal orbitals of pure Fe character, at given points of the Brillouin zone.

Figure 11. Scheme of the low-temperature structure of β-FeSe (*P4*/*nmm*) with edge-sharing $FeSe_4$ tetrahedra in the *ab* plane (left), and succession of layers along c (right).

Figure 11 shows the crystal structure of β-FeSe. The iron atoms form a square-plane network identical to the one for oxygen atoms in cuprates, as essential feature for our scenario of high-T_C superconductivity. However, the cationic vs. anionic character of Fe vs. O limits this analogy; in particular, the $E(q)$ curve for iron cannot show a minimum near q=2 (see Figure 8 for oxygen). Also, the cationic sites differ from an elongated octahedron (D_{4h}) or a pyramid (C_{4v}) in cuprates to a slightly elongated tetrahedron (T_d) in iron selenides or flattened iron pnictides. The tetrahedron distortion induces a degeneracy lift of iron t_2 orbitals into an *e* doublet (xz, yz) and a b_2 singlet (xy), only partly compensated by the crystal field (D_{4h}) of the four Fe^{n+} next-neighbors (at distance 2.67 Å).

Figure 12 shows the dispersion curves obtained from the tight-binding calculations for a Fe_2Se_2 primitive cell; the Fermi level is situated at -11.74 eV. Several band stacks can be identified, in order of increasing energy: i) around -21/-22 eV, two Se 4s-character bands (not represented in the figure); ii) between ca. -15.5 and -14 eV, six rather narrow Se 4p-character valence bands, with a significant Fe contribution; iii) broad conduction bands, divided in two stacks (according to the bonding or antibonding Fe-Fe interactions) that overlap slightly at Γ2 and M2 points, close to Fermi level. This creates two charge carrier pockets, of p type around Γ2 and n type around M2, with main components x^2-y^2 and (xz, yz). We observe that xy-character Fe-Fe bonding and antibonding bands are well separated, respectively below and above Fermi level, and corresponding to configurations $\sigma(b_2)^2$ and $\sigma^*(b_2)^0$.

The conduction band σ*(xz,yz) is broad (width > 3 eV); its top is strongly hybridized, with respective weights of 42 % and 58 % for Fe and Se, and its bottom is mostly of Fe character. It shows a progressive change into a broad domain (ca. 2 eV) with narrower bands built on Fe-Fe interactions. It is close to half-filling, leading to a xz^1yz^1 configuration of Pauli-type states.

The two x^2-y^2 bands, bonding and anti-bonding with respect to Fe-Fe interactions, are noted $1\pi_u$ and $1\pi_g$ respectively. Figure 13 represents an enlargement of Figure 12 around M2 and close to E_F, for the six bands arising from $1e_u$, $2e_u$ and $3e_u$, based on ($x^2 - y^2/4p_x$, $4p_y$), (xz, yz) and (xz, yz/$4p_z$) respectively. This corresponds to a $(x^2\text{-}y^2)^1$ configuration for Fe.

Two narrower d_{z2} bands are full, for a $(z^2)^2$ configuration. Overall, this is consistent with

divalent Fe, with xy and x^2-y^2 electrons providing the strong cohesion of the network (d_{Fe-Fe} = 2.67 Å, close to the distance observed in γ-Fe).

The hypothesis of a $1\pi_u^2 1\pi_g^0$ configuration corresponds to a very low *U* value. Otherwise, the spin polarization of these bands would induce a non-compensation magnetism, as observed in insulating phases of similar structure, with ordered Fe vacancies, such as $K_{0.8}Fe_{1.6}Se_2$ ($a\sqrt{5}$ x $a\sqrt{5}$, S.G. *I4/m*) in which ferromagnetic Fe_4 clusters order in an antiferromagnetic way below ca. 500 K [45].

The occurrence of Fe_4 clusters recalls the O_4 groups in cuprates, as discussed above. Furthermore, the low-temperature form of FeSe shows an orthorhombic distortion (S.G. *Cmma*, a/b = 0.9957) whose nematicity arises from the anisotropy of non-bonding Fe-Fe global interactions (antibonding along *a*, bonding along *b*) with a $a\sqrt{2}$ superstructure [19, 46]. This led us to extend our tight-binding calculations to a double unit cell.

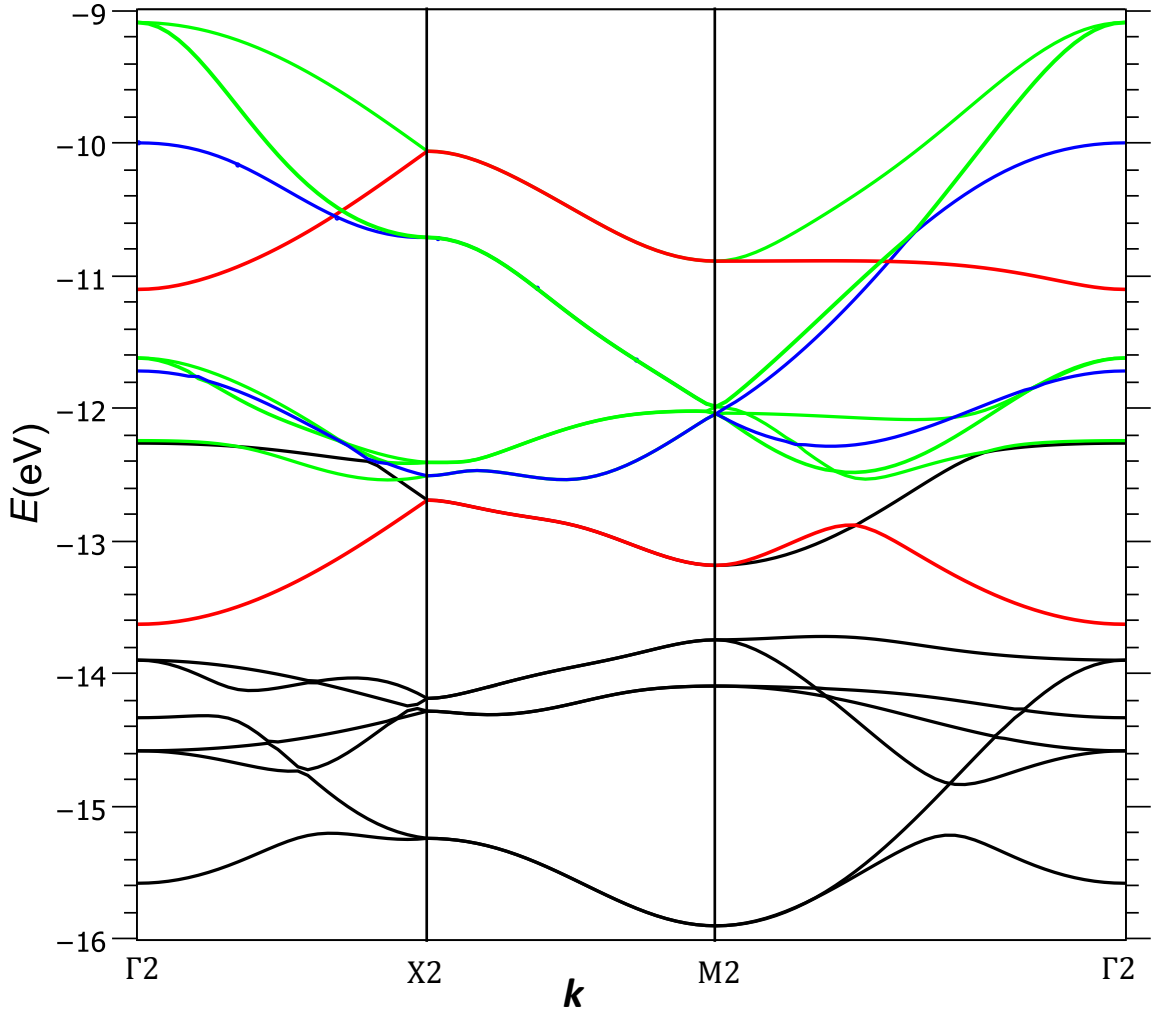

Figure 12. Dispersion curves $E(\boldsymbol{k})$ for the Fe_2Se_2 unit cell. Red: xy bands separated by a large gap between bonding and anti-bonding Fe-Fe interactions. Blue: (x^2-y^2) bands, degenerate at M2 point only. Green: conduction band based essentially on Fe (xz,yz) and Se 4p AOs.

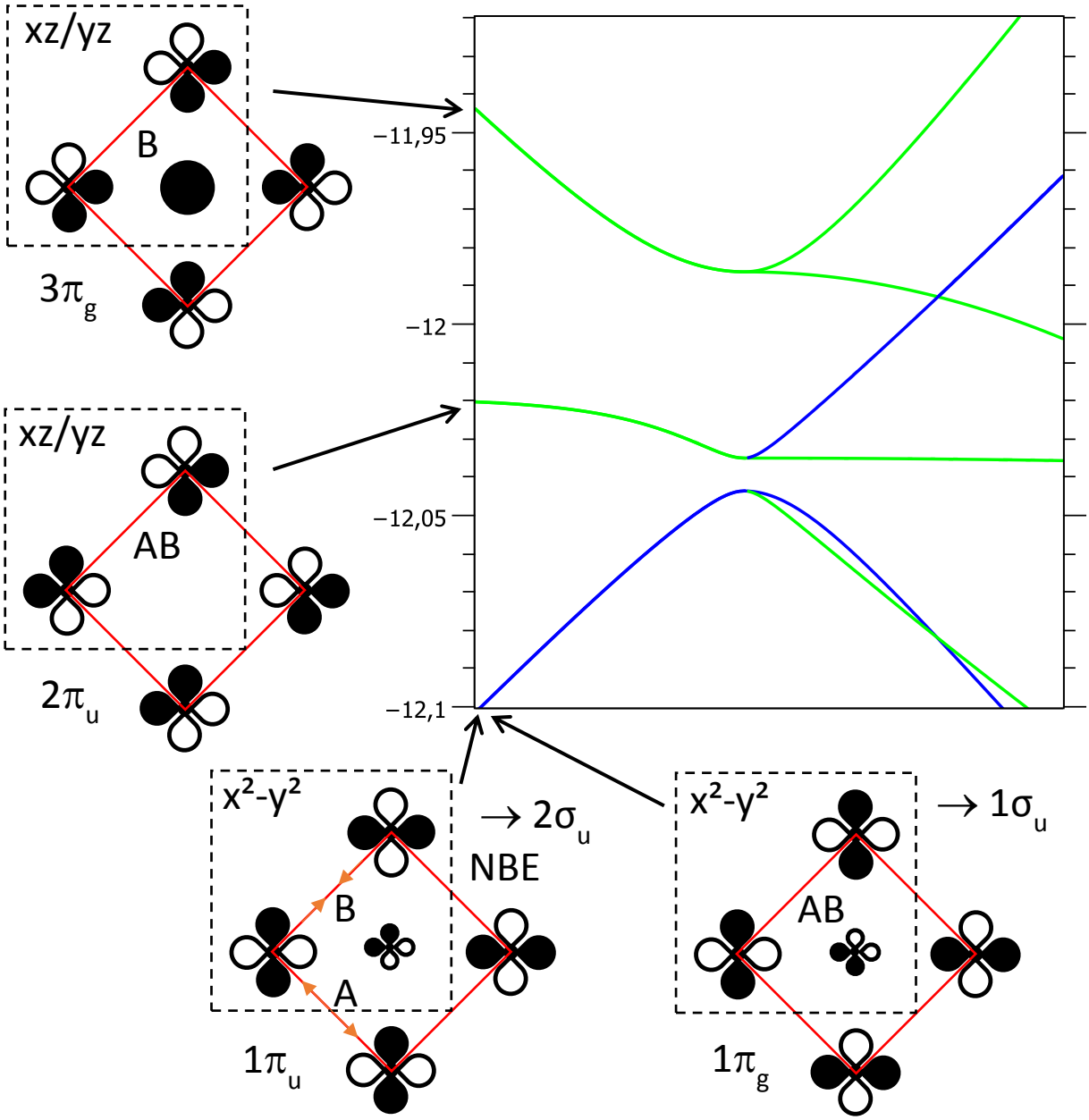

Figure 13. Enlargement of the DOS curves of Figure 12, around -12 eV, showing the three bands crossing at M2 ranked by increasing energy: $1\pi_g/1\pi_u$ ($1e_u$) in blue for x^2-y^2; $2\pi_g$ (not represented)/$2\pi_u$ ($3e_u$) in green for the xz,yz purely Fe-Fe AB interactions, and $3\pi_g/3\pi_u$ (not represented) ($3e_u$) mixed Se and Fe AOs (in green) with bonding Fe-Fe interactions in the broad conduction band. Note how $1\pi_g$ and $1\pi_u$ transform respectively in $1\sigma_u$ and $2\sigma_u$ for the double cell Fe_4Se_4.

The correspondences between CO notations in the single and double unit cells are given in Table 2.

Table 2. Correspondence table for the symmetry of crystal orbitals in FeSe, from single (Z = 2) to double unit cell (Z = 4), and two space groups for the latter.

Z = 2	Z = 4	
	P4/nmm	*Cmma*
$1e_u$	$1\pi_g$	$1\sigma_u$
	$1\pi_u$	$2\sigma_u$
$2e_u$	$2\pi_g$	$1\pi_u$
	$2\pi_u$	$2\pi_u$
$3e_u$	$3\pi_g$	$3\pi_u$
	$3\pi_u$	$4\pi_u$

We compare in the following the COs of such a double cell for the high temperature *P4/nmm* and the low temperature *Cmma* forms, the latter presenting a nematic distortion; we suppose a phonon regime where the parameter ratio a/b oscillates around 1, ($1\pm\delta$).

We focus our attention on the three degenerated COs in M_2, $1e_u$, $2e_u$ and $3e_u$ at respectively -12.044, -12.035 and -11.986 eV, and their six split bands towards Γ_4 (note that, for the double cell, x^2- y^2 is transformed into xy): (i) an AB hybridized Fe xy with Se $4p_x$ and $4p_y$ AOs in an orbital ordering way (O-O), noted $1e_u$ ($1\pi_g$, $1\pi_u \rightarrow 1\sigma_u$, $2\sigma_u$). Globally, Fe-Fe interactions are NB, the sum of B in *a* direction and AB in the *b* one, thus justifying the nematic instability. (ii) a purely Fe, $2e_u$ ($2\pi_g$, $2\pi_u \rightarrow 1\pi_u$, $2\pi_u$) band involving equally distributed weights of xz and yz on each Fe atom, AB arranged with the first neighbors and alternatively AB and B with the second ones. (iii) an AB hybridized Fe-Se, $3e_u$ ($3\pi_g$, $3\pi_u \rightarrow 3\pi_u$, $4\pi_u$) band, involving an (O-O), xz for the former and yz for the last one, mixed with Se $4p_z$ AOs; each coefficient c_i is close for each site. On the basis on degeneracies and regular weight distribution in the various sites, we cannot envisage any tendency of charge fluctuations, quoted here schematically "disproportionation", cationic as well as anionic, in the tetragonal phase.

What about the orthorhombic *Cmma* distortion? For a small iron atom displacement of $\pm$ 0.40 pm, the three band splitting in $\Gamma 4\ (= M2)$ are close to 15, 11 and 25 meV respectively, allowing thus to envisage a possible disproportionation.

(i) For the pure iron $2\pi_u/2\pi_g$ ($2e_u$) bands, we observe a (O-O) for yz and xz in the two bands; their mixing should only suppress such order.

(ii) For the Fe-Se hybridized xy (x^2-y^2), $1\sigma_u/2\sigma_u$ bands, their c_i coefficients are equally

distributed on each atom ($\pm$0.46 for Fe, $\pm$0.17 for Se) conserving (O-O). Distortion as well as iron oscillation apart their symmetrical positions (phonons) favoring as previously bonding along *a* (shortest Fe-Fe bonds) in $1\sigma_u$ and along *b* in $2\sigma_u$, changes some signs of AO coefficients. As for the corresponding band of cuprates (Figure 6a), at each half period fundamental state changes from $1\sigma_u$ to $2\sigma_u$, violating the NCR of chemistry. For avoiding that, the two bands do mix together, progressively up to a complete inversion, with three consequences:

- The creation of a "crystallographic" gap,
- Different sign for the coefficients in the four iron sites between $1\sigma_u$ and $2\sigma_u$ bands inverses their sum (Σ) or their difference (Δ),
- Passage during this mixture by an appropriated concentration of pair-occupied states and pair-empty states may induce superconductivity with a $2\Delta'$ SC gap [23].

Using the previous values of c_i, we obtained for Σ: $c_1 = c_2 = 0$; $c_3 = c_4 = \pm$ 0.46 for the lower 50:50 mixture (Figure 14), and for Δ: $c_1 = c_2 = \pm$ 0.46 and $c_3 = c_4 = 0$ for the upper. Two iron atoms over four carry charge densities on their xy (x^2-y^2) AOs corresponding to $4(x^2- y^2)^1 = 2(x^2-y^2)^2 + 2(x^2-y^2)^0$, or 4 Fe^{2+} = 2 Fe^{+} + 2 Fe^{3+}schematically quoted. Such a succession along [100] and [010] of "Fe^{+} "and "Fe^{3+} "allows the Cooper pairs formation and condensation at T_C (Figure 15).

Such a "disproportionation" is related to the Hubbard parameter *U* for Fe 3d orbitals and deals also with the difference between the third and the second ionization energies of Fe, which is the lowest (EI_3 - EI_2 = 14.5 eV) value for the M^{2+} 3d transition metal series, as shown in Table 3. However similar mixing between Se $4p_x$ and $4p_y$ AOs does not show any charge fluctuations in this $1\sigma_u/2\sigma_u$ band.

Table 3. Values of second and third ionization energies of some transition metals, and their difference (in eV).

	Cr	Mn	Fe	Co	Ni	Cu	Zn
IE_2	16.49	15.64	16.19	17.08	18.17	20.29	17.96
IE_3	30.96	33.67	30.65	33.50	35.19	36.84	39.72
IE_3-IE_2	14.47	18.03	14.46	16.42	17.02	16.55	21.76

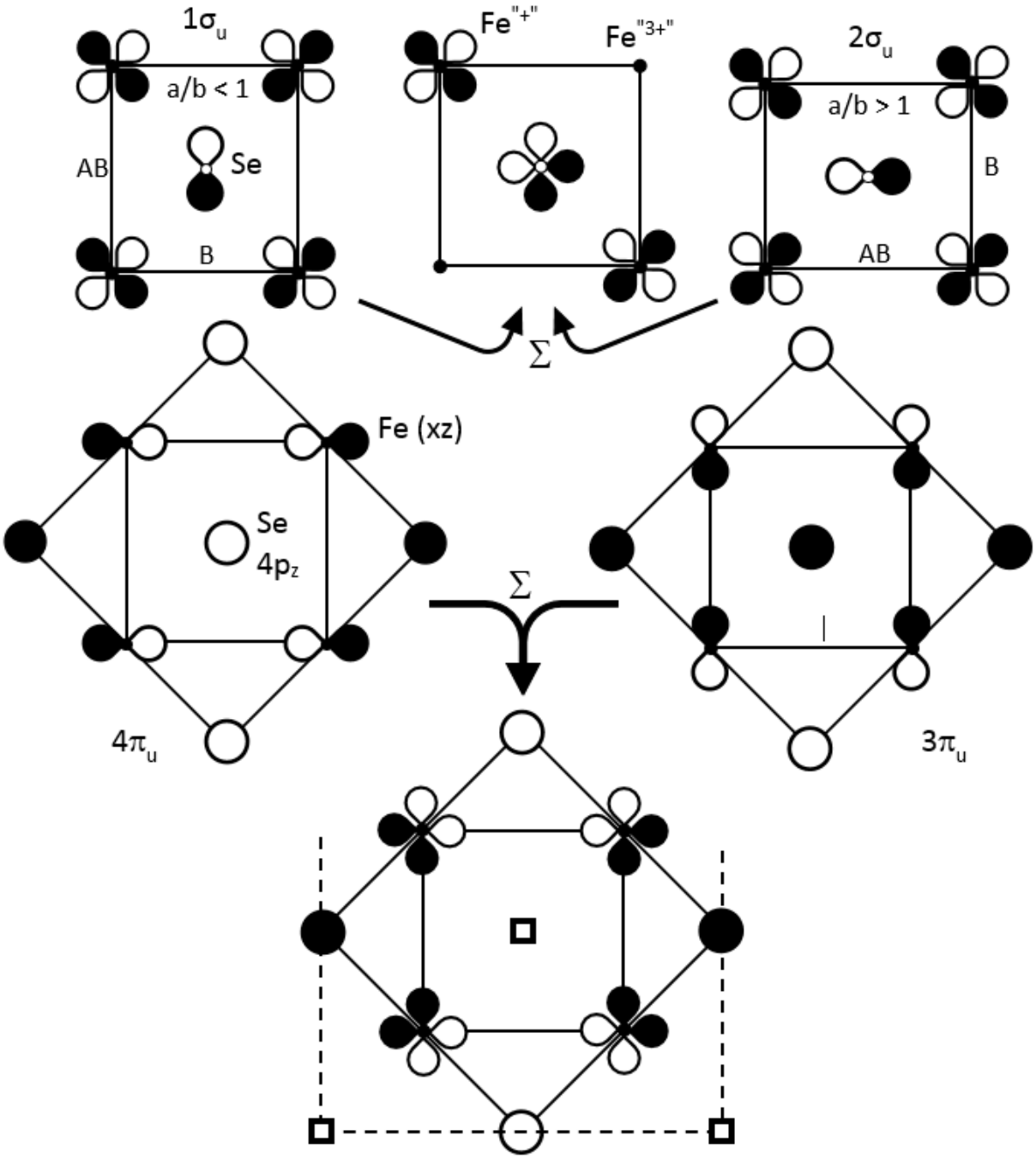

Figure 14. Orthorhombic *Cmma* distortion of the tetragonal Fe_4Se_4 double cell showing: i) a nematic distortion along the corresponding phonon mode (see Figure 6), for $1\sigma_u$ (a/b < 1 and B > AB on the left) and $2\sigma_u$ (a/b > 1 and B > AB on the right). $1\sigma_u$ and $2\sigma_u$ should mix during this inversion step, when the gap becomes smaller and smaller. The upper part shows the 50:50 mixing; from the AO coefficients in the two bands, two among four Fe atoms do not participate to the mixed wave function. This large charge fluctuation can be schematized as a phonon-induced "disproportionation" state implying electron-pair exchange. As shown in the lower part, the same distortion implies conversely, for $3\pi_u/4\pi_u$ ($3e_u$) mixing, a "disproportionation" state for Se atoms. Note that Se atoms lie above and below the Fe plane (see Figure 11); one layer over two only contributes to the wave function.

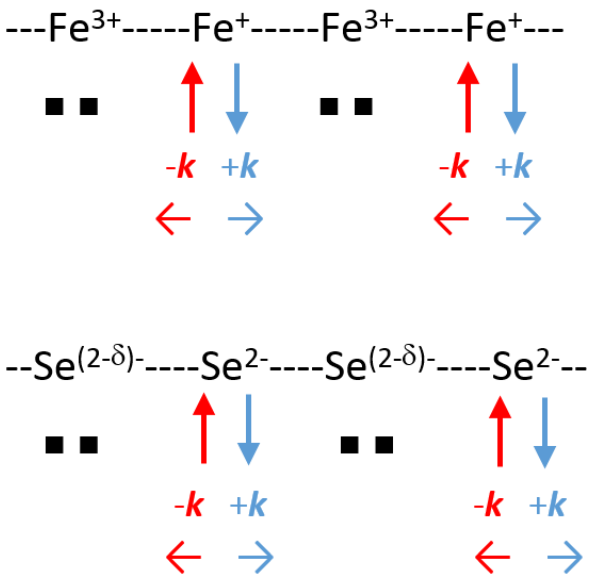

Figure 15. Top: Fe charge disproportionation in the C*mma* unit cell of FeSe (Z = 4), by $1\sigma_u$-$2\sigma_u$ mixing along [100] and [010]. Bottom: charge fluctuation between successive (001) planes of selenium atoms, by $3\pi_u$-$4\pi_u$ mixing. Fe disproportionation and Se charge fluctuation are both consequences of the non-crossing rule.

Besides, the highly split $3e_u$ ($4\pi_u/5\pi_u$) belonging to the bottom of the large conduction band with xz/yz (O-O) (Figure 13), and so inactive by mixing for iron disproportionation, differentiate two over four selenium positions, up and down from the iron layer: $c_1(\Sigma) = -c_2(\Sigma) = 0.20$; $c_3(\Sigma) = c_4(\Sigma) = 0$ and $c_1(\Delta) = c_2(\Delta) = 0$; $c_3(\Delta) = -c_4(\Delta) = 0.20$.

Each of them forms a square lattice of $a/\sqrt{2}$ parameter (tetrahedron edge) up and down of the iron layer with π- AB Se-Se interactions . At Γ point these interactions add to those of Fe-Se AB character for destabilizing the top of the occupied states, favoring CT. As discussed previously for cuprates (Figure 8) for the $E(q)$ curve of oxygen, strong similarities are observed for selenium; the created holes can be associated in pairs and the mixing of the $3\pi_u/4\pi_u$ bands can also contribute to the $2\Delta'_{SC}$ superconducting gap as above (Figure 15)

Thus, the Fe-Se system disposes of two, cationic and anionic, phonon coupled drivers for associating carriers in pairs and condensing them in Cooper pairs below T_C.

Similarly to the case of p-doped cuprates, we examine in which way the Fermi level could shift by a hundred meV to reach the M_2 (x^2-y^2) point: this would be achieved through an electron transfer from $(x^2-y^2)^*$ to $(xz, yz)^*$ bands, i.e. from σ to π, the latter being more stabilized by the intercalation of cations in the inter-layer space, as demonstrated by Pickett et An for MgB_2 vs. graphite [47]. The 30 K superconductors $A_{0.6}Fe_2Se_2$ ($A=M^+$) illustrate such behavior,

increasing Fe^{+} rate and consequently Fermi energy, but conversely stabilizing π*(xz,yz) versus σ*(x^2-y^2) as previously [48].

6. Methods

Tight-binding calculations were done using the Extended Hückel method [49-52], as implemented in the CAESAR package [53], using parameters listed in Table 1.

7. Conclusion

The answer to the question in the title is clear: we believe that chemical bonding is at the heart of physical ordering phenomena and contributes to the understanding of non-conventional, high-T_C superconductivity mechanisms. It sheds light on the key role of non-bonding electrons (NBE), from which an electronic instability occurs through a double-well situation, inducing a static or dynamic (phonons) distortion of the atomic network. The couple NBE + phonons is the core of our chemists' approach.

At low temperature, the softening of phonons leads to a succession of symmetry broken and non-broken states, i.e. the alternation of an insulating distorted phase and a metallic phase. Importantly, it is also at the origin, on a shorter timescale, of a superconducting phase in which the mixing of occupied and unoccupied electron-pair states (described by Whangbo in Ref. 23) can be achieved through a purely electronic Hamiltonian. This situation avoids the non-crossing rule for band-edge states, which should swap at each phonon half-period.

Besides, the approach of Micnas et al., based on the mixing of local pairs and itinerant electrons (when wide and narrow bands cross at Fermi level) giving rise to a mutually induced superconductivity, is also relevant for our model.

The whole scheme applies to the three families of solids discussed here:

i) titanates, in which the top of the valence band is non-bonding and induces both a ferroelectric-type distortion, the splitting of the π*(t_{2g}) band into a narrow 2D band of b_{2g} symmetry (xy) and a broader 3D band of e_g symmetry (xz, yz),

ii) cuprates (at optimal p doping) have a wide conduction band, of oxygen character and σ*(b_{1g}) symmetry, with a 2D Peierls-type instability for non-bonding electrons at the band center. This instability is probably of dynamical nature, and occurs at Fermi level at the vicinity of a narrow band of pure oxygen character and of π*(a_{2g}) symmetry;

iii) β-FeSe and iron pnictides of similar crystal structure have a broad conduction band (due to the strong Se (4p) - Fe (xz, yz) hybridization) and, close to Fermi level, a much narrower band of Fe character, likely to split from a non-bonding situation into two (x^2-y^2)-character bands, respectively Fe-Fe bonding and antibonding.

In each family, the occurrence of bosonic local pairs is favored by specific features, respectively:

i) a high dielectric constant that minimizes the Coulomb repulsion between the two electrons of the b_{2g}^2 local pair ($U \rightarrow 0$),

ii) the occurrence of a poly-oxyde (even peroxyde) cluster $(O_4)^{n-}$, favored both by the almost constant formation energy of the O^{-q} ion for charges q between -1 and -1.5, a large transfer integral t_{o-o} for hole delocalization, and the local crystal field at the copper-free(+) site, leading to a negative *U* situation,

iii) the existence of two (x^2-y^2) sub-bands by splitting of $1e_u$ in *Cmma*, of NB Fe-Fe character with Fe +II large charge fluctuations, crossing a broad 3D band of (xz,yz) character and strongly hybridized with the chalcogen. As for oxygen atoms in cuprates, the anionic Se layer undergoes also similar charge fluctuations, likely coupled together.

These situations agree perfectly with the requirements of the negative *U* pairing mechanism, i.e. quasi degenerate states, same coordination and hybridization with the conduction band, as recently reported by Geballe, Hammond and Wu in a general introduction of superconductivity mechanisms [36].

The antagonism between several types of order can be discussed, magnetism vs. superconductivity, and magnetism vs. charge transfer: i) as well known, magnetism destroys superconductivity above a critical field value, but the magnetic ordering is itself destroyed by charge transfer arising from p-doping in Cu +II cuprates, leading eventually to a collapse of T_C. However, both appear to be at the origin of superconductivity of under-doped cuprates, as well as their stripe-type insulating phases. ii) Ferroelectricity and superconductivity seem to be incompatible, despite a few exceptions (see the discussion in Ref. 16), because a significant carrier density is required (Mott transition). However, Rischau's works [15] suggest that ferroelectric-type distortions woos as well to electron pairing.

For both apparent antagonisms, the chemist' toolbox provides key arguments for possible interpretations.

Finally, the general model proposed here appears as a coherent mixture of parts of physics and parts of chemistry: (i) the phonon role, alternating broken and unbroken symmetry, (ii) the broad and narrow band crossing of Micnas et al., (iii) the negative *U* Hubbard model, as ingredients of the BCS theory, for physics, (iv) the non- bonding electron instability, (v) the non- crossing rule of states and bands, and (vi) the charge-transfer disproportionation (which is equivalent to negative *U*), for chemistry. In addition, chemistry also suggests that anionic hybridization like $O_{2p} \pm O_{2s}$ AOs, rejecting alternatively electron densities on both sides from the symmetry center, describes very well the atomic polarizability and could be an high-frequency alternative to phonons. In addition, coupling cationic and anionic disproportionation could enhance superconductivity as observed in cuprates and selenides.

References

1 Schafroth, M.R.; Blatt, J.M.; Butler, S.T. *Helv. Phys. Acta* **1957**, *30*, 93.

2 Little, W.A. *Phys. Rev. A* **1964**, *134*, 1416.

3 Bardeen, J.; Cooper, L.; Schrieffer, J. *Phys. Rev.* **1957**, *108*, 1175.

4 Pouchard, M.; Launay, J.C. *Mater. Res. Bull.* **1973**, *8*, 95.

5 Chevrel, R.; Sergent, M.; Prigent, J. *J. Solid State Chem.* **1971**, *3*, 515.

6 Matthias, B.T.; Marezio, M.; Corenzwit, E.; Cooper, A.S.; Barz, H.E. *Science* **1972**, *175*, 1465.

7 Goodenough, J. B.; Demazeau, G.; Pouchard, M.; Hagenmuller, P.; *J. Sol. State Chem.* **1973**, *8*, 325.

8 Bednorz, J.G.; Müller, K.A. *Z. Phys. B: Condens. Matter* **1986**, *64*, 189.

9 Nguyen, N. ; Studer, F. ; Raveau, B. *J. Phys. Chem. Solids* **1983**, *44*, 389.

10 Pouchard, M.; Grenier, J.C.; Doumerc, J.P. *C. R. Acad. Sc.* **1987**, *305*, 571.

11 Simon, A. *Angew. Chem.* **1987**, *99*, 602.

12 Sleight, A.W. *Chemtronics* **1987**, *2*, 116.

13 Micnas, R.; Ranninger, J.; Robaczkiewicz, S. *Rev. Mod. Phys.* **1990**, 62, 113.

14 Simon, A. *Angew. Chem. Int. Ed. Engl.* **1997**, *36*, 1788.

15 Rischau, C.W.; Lin, X.; Grams, G.P.; Finck, D.; Harms, S.; Engelmayer, J.; Lorenz, T. *Nature Physics* **2017**, *13*, 643.

16 Gabay, M.; Triscone, J.M. *Nature Physics* **2017**, *13*, 624.

17 Pouchard, M. ; Villesuzanne, A. http:/arxiv.org/abs/1707.00870

18 Hosono, H.; Kuroki, K. *Physica C* **2015**, *514*, 399.

19 Chang, C.C.; Chen, T.K.; Lee, W.C.; Lin, P.H.; Wang, M.J.; Wen, Y.C.; Wu, P.M.; Wu, M.K. *Physica C* **2015**, *514*, 423.

20 Wheeler, R.A.; Whangbo, M.H.; Hughbanks, T.; Hoffmann, R.; Burdett, J.K.; Albright, T. *J. Am. Chem. Soc.* **1986**, *108*, 2222. Albright, T.A.; Burdett, J.K.; Whangbo, M.H. *Orbitals interactions in Chemistry*. John Wiley et Sons **1985**.

21 Deutscher, G.; de Gennes, P.G. *C. R. Physique* **2007**, *8*, 937.

22 Orgel, L.E. *J. Chem. Phys.* **1955**, *23*, 1004.

23 Whangbo, M.H. *Electron Transfer in Biology and the Solid State.* American Chemical Society **1990**.

24 Hagenmuller, P. Non-Stoichiometric Compounds, Pergamon Oxford, (1975).

25 Edwards, P.P.; Sienko, M.J. *J. Am. Chem. Soc.* **1981**, *103*, 2967.

26 Gariglio, S.; Gabay, M.; Mannhart, J.; Triscone, J.M. *Physica C* **2015**, 514, 189.

27 Clementi, E.; Roetti, C. *At. Data Nucl. Data Tables* **1974**, 14, 177.

28 Demazeau, G.; Parent, C.; Pouchard, M.; Hagenmuller, P. *Mater. Res. Bull.* **1972**, *7*, 913.

29 Pouchard, M.; Doumerc, J.P. ; Villesuzanne, A. *Inorg. Chem.* **2008**, 47, 8487.

30 Bianconi, A. et al. *Phys. Letter A* **1988**, *127*, 285.

31 Mehta, A.; Carlo, J.D. Navrotsky, A. *J. Solid State Chem.* **1992**, *101*, 173.

32 Hanaguri, T.; Lupien, C.; Kohsaka, Y.; Lee, D.H.; Azuma, M.; Takano, M.; Tagaki, H.; Davis, J.C. *Nature* **2004**, *430*, 1001.

33 Koshaka, Y. et al. *Science* **2007**, *315*, 1380.

34 Pasupathy, A.N. et al. *Science* **2008**, *320*, 11958.

35 Jurkutat, M. et al. in *High-T_C copper oxide superconductors and related novel materials*, Bussmann-Holder, A.; Keller, H.; Bianconi, A. *Springer Series in Materials Science* **2017**, *255*, 77-87.

36 Geballe, T.H.; Hammond, R. H.; Wu, P.W. *Physica C* **2015**, *514*, 9.

37 Hirsch, J.E. *Solid State Comm.* **1989**, 69, 987; *Phys. Rev. Lett.* **2001**, *87*, 206402

38 Villesuzanne, A. ; Pouchard, M. *C. R. Acad. Sci. Paris Ser. IIb* **1996**, *322*, 155.

39 Zhang, F.C.; Rice, T.C. *Phys. Rev. B* **1988**, *37*, 3759.

40 Badoux, S. et al. *Nature* **2016**, *531*, 210.

41 Reznick, D. et al. *Nature* **2006**, *440*, 1170.

42 Bertaut, E.F.; Burlet, P.; Chappert, J. *Solid State Comm*. **1965**, *3*, 335.

43 Kamihara, Y.; Watanabe, T.; Hirano, M.; Hosono, H. *J. Am. Chem. Soc.* **2008**, *130*, 3296.

44 Gütlich, P. *Spin Cross-over in Iron(II)-Complexes.* Springer, *Structure and Bonding* **1981**, *44*.

45 Khasanov, R.; Bendele, M.; Conder, K.; Keller, H.; Pomjakushina, E.; Pomjakushin, V. *New J. Phys.* **2010**, *12*, 073024.

46 Bao, W.; Huang, Q.Z.; Chen, G-F.; Green, M.A.; Wang, D.-M.; He, J.-B.; Qiu, Y.-M. *Chin. Phys. Lett.* **2011**, *28*, 086104.

47 An, J.M.; Pickett, W.E. *Phys. Rev. Lett.* **2001**, *86*, 19, 4366.

48 Shoemaker, D.P.; Chung, D.Y.; Klaus, H.; Francisco, M.C.; Avci, S.; Llobet, A.; Kanatzidis, M.G. *Phys. Rev. B* **2012**, *86*, 184511.

49 Hoffmann, R. *J. Chem. Phys.* **1963**, 39, 1397.

50 Whangbo, M.-H.; Hoffmann, R. *J. Am. Chem. Soc.* **1978**, 100, 6093.

51 Ammeter, J.H.; Bürgi, H.B.; Thibeault, J.C.; Hoffmann, R. *J. Am. Chem. Soc.* **1978**, 100, 3686.

52 Wolfsberg M.; Helmholz, L. *J. Chem. Phys.* **1952**, 20, 837.

53 CAESAR program package (Ren, J.; Liang, W.; Whangbo, M.-H. **1998**). This package can be downloaded free of charge from the website, http://www.primec.com/